

Encoded probabilistic imaginary-time evolution on a trapped-ion quantum computer for ground and excited states of spin qubits

Hirofumi Nishi^{1, 2, *} Yuki Takei,^{3, 4} Taichi Kosugi^{1, 2} Shunsuke Mieda,^{3, 4}
Yutaka Natsume,^{4, 3} Takeshi Aoyagi^{1, 4} and Yu-ichiro Matsushita^{1, 2, 1, 5, 6}

¹Quemix Inc., Taiyo Life Nihombashi Building, 2-11-2, Nihombashi Chuo-ku, Tokyo 103-0027, Japan

²Department of Physics, The University of Tokyo, Tokyo 113-0033, Japan

³Platform Laboratory for Science & Technology, Asahi Kasei Corporation,

2-1, Samejima, Fuji, Shizuoka, 416-8501, Japan

⁴Informatics Initiative, Asahi Kasei Corporation,

3-1-1 Shibaura, Minato-ku, Tokyo, 108-0023, Japan

⁵Quantum Materials and Applications Research Center,

National Institutes for Quantum Science and Technology (QST),

2-12-1 Ookayama, Meguro-ku, Tokyo 152-8550, Japan

⁶Laboratory for Materials and Structures, Institute of Innovative Research,

Tokyo Institute of Technology, Yokohama 226-8503, Japan

(Dated: July 16, 2024)

In this study, we employed a quantum computer to solve a low-energy effective Hamiltonian for spin defects in diamond (so-called NV centre) and wurtzite-type aluminium nitride, which are anticipated to be qubits. The probabilistic imaginary-time evolution (PITE) method, designed for use in a fault-tolerant quantum computer (FTQC) era, was employed to calculate the ground and excited states of the spin singlet state, as represented by the effective Hamiltonian. It is difficult to compute the spin singlet state correctly using density functional theory (DFT), which should be described by multiple Slater determinants. To mitigate the effects of quantum errors inherent in current quantum computers, we implemented a $[[n+2, n, 2]]$ quantum error detection (QED) code called the Iceberg code. Despite the inevitable destruction of the encoded state resulting from the measurement of the ancilla qubit at each PITE step, we were able to successfully re-encode and recover the logical success state. In the implementation of the PITE, it was observed that the effective Hamiltonian comprises large components of the diagonal part and a relatively small non-diagonal part, which is frequently the case with quantum chemistry calculations. An efficient implementation of Hamiltonian simulations, in which the diagonal components dominate, was developed on a quantum computer based on the second-order Trotter-Suzuki decomposition. This is the first instance of an encoded PITE circuit being executed on a trapped-ion quantum computer. Our results demonstrate that QED effectively reduces quantum errors and that we successfully obtained both the ground and excited states of the spin singlet state. Our demonstration clearly manifests that $\text{Zr}_{\text{Al}}\text{V}_\text{N}$, $\text{Ti}_{\text{Al}}\text{V}_\text{N}$, and $\text{Hf}_{\text{Al}}\text{V}_\text{N}$ defects have a high potential as spin qubits for quantum sensors.

I. INTRODUCTION

The field of quantum technology has made noteworthy advancements in recent years, with notable developments observed in areas including computing, sensing, and communications. In particular, the application of quantum computers in material calculations offers the promise of performing highly accurate simulations of molecular and material properties, which are crucial for understanding and designing new materials. Hamiltonian simulation [1–7] enables the modelling of a system’s quantum behaviour, thereby facilitating insights into its dynamics and interactions. Quantum phase estimation (QPE) is indispensable for determining the eigenvalues of Hamiltonians, which are directly related to the ground state energy of the system [8–11]. Efficient state preparation is a prerequisite for QPE, and a number of approaches

have been proposed, including adiabatic time evolution [12–15], variational quantum eigensolver (VQE) [16, 17], quantum eigenvalue transformation of unitary matrices (QETU) [18], and imaginary-time evolution (ITE) on quantum computers [19–25]. These algorithms can be used to calculate a variety of physical quantities as key components [26–29].

In recent years, there has been a substantial increase in the number of qubits for various physical platforms, including superconductivity [30–32], trapped ions [33, 34], and neutral atoms [35–37]. As a result of the limitations of noisy intermediate-scale quantum (NISQ) devices and the increasing number of qubits, there has been a growing interest in demonstrating error-corrected logical qubits and logical gate operations [36, 38–40]. These developments are pushing the boundaries of what is possible with current technology. Furthermore, quantum computer hardware can now be accessed via the cloud, thereby facilitating its utilisation by theoretical scientists and materials companies [41]. This has led to a proliferation of research papers and significant advancements in

* hnishi@quemix.com

this field [25, 42–46].

On the other hand, spin defects in wide-gap semiconductors are attracting attention as promising quantum sensing materials because of their high sensitivity to magnetic fields, capability of room-temperature operation, and tolerance to extreme environments, such as radiation and high temperatures and pressures. In particular, the negatively charged nitrogen vacancy, the so-called NV[−] center in diamond [47, 48], which exhibits the highest magnetic field sensitivity, has already been reported to have various applications, such as magnetoencephalography and temperature measurement of local regions within cells. Silicon carbide (4H-SiC), which is increasingly being applied as a power device [49–52], is also known to be able to create qubits compatible with room-temperature operation [53–58] and is attracting attention because of its ability to manufacture and process high-purity crystals. Similarly, ultrahigh-purity crystal growth [59–61] and doping [62] are possible with wurtzite-type aluminum nitride (w-AlN), which has a wide band gap i.e., 6.12 eV, [63] and is attracting attention as a host material for spin qubits. First-principles calculations have theoretically predicted that complex defects such as (Zr_{Al}V_N)⁰, (Hf_{Al}V_N)⁰, and (Ti_{Al}V_N)⁰ are promising candidates for spin qubits [64, 65].

In this study, we employed the probabilistic imaginary-time evolution (PITE) [23], an algorithm that has been demonstrated to provide quantum acceleration for ground state preparation [66], to simulate the electronic structure of spin defects on Quantinuum trapped-ion quantum computer [38, 67, 68]. In order to account for spin defects in the crystals, including NV[−] center in diamond and complex defects in w-AlN [64, 65], we constructed a low-energy effective Hamiltonian [69, 70]. It is established that the singlet states of NV[−] center in diamond are multi-configuration states, rendering them challenging to describe using the density functional theory (DFT) [71, 72] framework, which is formulated based on a single Slater determinant. The PITE method was employed for the low-energy effective Hamiltonian, thereby enabling an accurate description of the singlet states of the NV[−] center in diamond. This methodology will facilitate the discovery of a new spin defect for quantum sensing materials.

Quantinuum H1-1 computer has high-fidelity two-qubit gate of $\sim 2.0 \times 10^{-3}$ infidelity with the all-to-all connectivity, performs mid-circuit measurement, and presents quantum volume of 2²⁰. However, the remaining quantum errors may worsen the computed results, and we address this issue by implementing quantum error detection (QED) [38, 73–76]. In particular, we employed the Iceberg code [38], which requires only four ancilla qubits for encoding and syndrome measurements. In QED, ancilla qubits are employed for each cycle of syndrome measurement, similarly in PITE, ancilla qubits are utilised for each cycle of the small imaginary time evolution. The feature of the Quantinuum H1-1 computer, which performs mid-circuit measurement and reuse, is

desirable for executing QED and PITE.

II. METHOD

A. An low-energy effective model of the spin-defect qubits

1. DFT calculation

DFT calculations were performed using a plane-wave basis set and optimized norm-conserving Vanderbilt pseudopotentials [77–79] as implemented in the Quantum ESPRESSO code [80–82]. First, the structure of the complex defects in the supercell was optimized using spin-polarized DFT calculations with Perdew-Burke-Ernzerhof (PBE) semilocal functional [83] until all forces were smaller than 10^{−3} a.u.. As a result of confirming convergence in Appendix A, we adopted an energy cutoff of 50 Ry and a supercell of 216 atoms for the NV[−] center in diamond, and an energy cutoff of 75 Ry and a supercell of 240 atoms for the complex defects in w-AlN. We confirmed the convergence of the energy cutoff within 113 meV and 1.9 meV for the NV[−] center in diamond and complex defects in w-AlN by calculating the same system with an energy cutoff of 100 Ry, respectively. Brillouin zone, we employed Γ point in both systems. We employed Γ point sampling for the Brillouin zone in both systems. To obtain the wave function for constructing a low-energy effective model, DFT calculations with the screened hybrid functional of Heyd-Scuseria-Ernzerhof (HSE) [84, 85] were performed.

2. A low-energy effective model

In this study, in order to accurately describe phenomena in the low-energy region, we construct the extended Hubbard model given by

$$\mathcal{H} = \sum_{\sigma} \sum_{ij} t_{ij} a_{i\sigma}^{\dagger} a_{j\sigma} + \frac{1}{2} \sum_{\sigma\rho} \sum_{ij} \left[U_{ij} a_{i\sigma}^{\dagger} a_{j\sigma}^{\dagger} a_{j\rho} a_{i\sigma} + J_{ij} (a_{i\sigma}^{\dagger} a_{j\rho}^{\dagger} a_{i\rho} a_{j\sigma} + a_{i\sigma}^{\dagger} a_{i\rho}^{\dagger} a_{j\rho} a_{j\sigma}) \right], \quad (1)$$

where $a_{i\sigma}^{\dagger}$ and $a_{i\sigma}$ denote the creation and annihilation operators, respectively, of an electron with spin σ in the i th Wannier orbital, respectively. A transfer integral t_{ij} is defined as

$$t_{ij} = \langle \phi_i | \mathcal{H}_0 | \phi_j \rangle \quad (2)$$

where $|\phi_i\rangle$ denotes the spatial part of the wave function created by a_i^{\dagger} . \mathcal{H}_0 represents the one-body Hamiltonian, here we take it as Kohn-Sham (KS) Hamiltonian \mathcal{H}_{KS} computed in previous subsection. The screened-Coulomb U_{ij} and exchange J_{ij} integrals are given by

$$U_{ij}(\omega) = \langle \phi_i \phi_j | W(\omega) | \phi_i \phi_j \rangle \quad (3)$$

and

$$J_{ij}(\omega) = \langle \phi_i \phi_j | W(\omega) | \phi_j \phi_i \rangle, \quad (4)$$

where $W(\omega)$ denotes the frequency-dependent screened Coulomb interaction based on constrained random phase approximation (cRPA). The static limit of the screened Coulomb integrals is used to describe the interaction in the Hamiltonian:

$$U_{ij} = \lim_{\omega \rightarrow 0} U_{ij}(\omega) \quad (5)$$

and

$$J_{ij} = \lim_{\omega \rightarrow 0} J_{ij}(\omega). \quad (6)$$

Note that a methodology to remove double counting of two-electron integrals from the one-electron integral was proposed [86]; however, we ignored double counting because the effect on the full-configuration interaction (FCI) energy is negligible in this study.

In this study, the direct Coulomb and exchange integrals were calculated using the software RESPACK [87]. We used the cutoff energy for the polarization function $E_{\text{cut}}^{\epsilon}$ of 3.0Ry and 4.5Ry for NV⁻ center in diamond and complex defects in w-AlN, respectively. We used KS energy levels N_{band} of 750 and 1300 for NV⁻ center in diamond and complex defects in w-AlN, respectively. In Appendix A, it is confirmed that the energy of the FCI calculation converges by taking the value $E_{\text{cut}}^{\epsilon}$ of 6% of the energy cutoff of the DFT calculation and by including conduction bands greater than 10 eV from the valence band maximum (VBM).

We define a linear transformation between Wannier orbitals and KS orbitals such that $a_i = \sum_j U_{i,j} c_j$, where c_j denotes the annihilation operator of the KS-basis. j for c_j is the composite notation for the wave vector and band index of the KS basis. Using the linear transformation, the Hamiltonian based on the KS orbitals is given by

$$\mathcal{H} = \sum_{\sigma} \sum_{i,j} \varepsilon_i^{\text{KS}} c_{i\sigma}^{\dagger} c_{i\sigma} + \frac{1}{2} \sum_{\sigma\rho} \sum_{i,j,k,l} \tilde{v}_{ijkl} c_{i\sigma}^{\dagger} c_{j\rho}^{\dagger} c_{l\rho} c_{k\sigma}. \quad (7)$$

Each interaction term in Eq. (7) involves four distinct KS orbitals, leading to $O(n^4)$ scaling for n Wannier orbitals. This is in contrast to the original Hamiltonian based on the Wannier basis in Eq. (1) with $O(n^2)$ scaling. As described below, we used the \mathbb{Z}_2 symmetry to reduce the number of qubits necessary. However, the \mathbb{Z}_2 symmetry cannot be used for the Wannier-basis representation; therefore, we converted it to the KS-basis representation in this study.

3. Spin operator representation

To implement the ITE of fermionic operators on a quantum computer, the transformation of fermionic op-

erators to Pauli operators is necessary [88–90]:

$$\mathcal{H} = \sum_{\ell=1}^{N_{\text{term}}} h_{\ell} P_{\ell}, \quad (8)$$

where h_{ℓ} denotes the real coefficients, and P_{ℓ} is the Pauli operator acting on some of n qubits. Here, we utilize parity transformation [90] for the low-energy effective Hamiltonian based on the KS orbitals. By indicating the parity of the total number of up and down spins, the parity transformation can reduce the number of qubits necessary by two.

Further qubit reduction is achieved by using \mathbb{Z}_2 symmetry[91]. This function identifies a Pauli operators P_{Z_2} such that $[P_{Z_2}, \mathcal{H}] = 0$. If we find such a Pauli operator, the eigenstates of the Pauli operator can be classified as either +1 or -1 eigenspace. In other words, it becomes possible to reduce the degree of freedom by one qubit.

B. Probabilistic imaginary-time evolution with Iceberg code

1. Probabilistic imaginary-time evolution

In this study, we adopted the PITE method [23] to obtain the lowest energy state among eigenvectors included in an initial state. After determining the ground state, the ground-state energy can be efficiently estimated using QPE [2, 8, 92–95]. For the Hamiltonian \mathcal{H} for an n -qubit system, we define a nonunitary Hermitian operator $\mathcal{M} := m_0 e^{-\mathcal{H}\Delta\tau}$, where $\Delta\tau$ denotes a small imaginary time-step size, and an adjustable real parameter m_0 satisfying $0 < m_0 < 1$, $m_0 \neq 1/\sqrt{2}$ is introduced. Introducing an ancilla qubit to embed the nonunitary operator as a submatrix into an extended unitary matrix, we have an entanglement state of the nonunitary operator acted (success state) and other state (failure state) for an input state $|\psi\rangle|0\rangle$, $|\psi\rangle|0\rangle \rightarrow \mathcal{M}|\psi\rangle|0\rangle + \sqrt{1 - \mathcal{M}^2}|\psi\rangle|1\rangle$. Measuring the ancilla qubit as $|0\rangle$ state with probability $P_0 = \langle\psi|\mathcal{M}^2|\psi\rangle$ collapses the entanglement state into the success state.

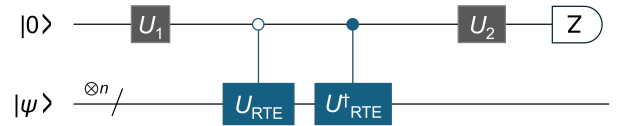


FIG. 1. Circuit diagram of the logical approximated PITE operator.

A previous study [23] proposed an approximate implementation method for the nonunitary operator \mathcal{M} within the first order of $\Delta\tau$. The approximated ITE operator is given by

$$\mathcal{M} = \sin(-\mathcal{H}\Delta\tau s_1 + \varphi) + O(\Delta\tau^2), \quad (9)$$

where $s_1 = m_0/\sqrt{1-m_0^2}$ and $s_1 = \tan \varphi$. The quantum circuit for the approximated PITE is shown in Figure 1. The quantum circuit is comprising of two single-qubit unitary operators $U_1 = R_Z(\pi/2)R_Y(\pi)R_Z(-\pi)$ and $U_2 = R_Z(\pi/2)R_Y(\pi)R_Z(2\theta_0 - 3\pi/2)$, and forward- and backward-controlled real-time evolution (CRTE) operators, $e^{\Delta\tau s_1 \mathcal{H}} \otimes |0\rangle\langle 0| + e^{-\Delta\tau s_1 \mathcal{H}} \otimes |0\rangle\langle 0|$ for time $\Delta\tau s_1$, where $\theta_0 = \kappa \arccos[(m_0 + \sqrt{1-m_0^2})/\sqrt{2}]$ and $\kappa = \text{sgn}(m_0 - 1/\sqrt{2})$.

2. Iceberg code

The Iceberg code encodes k even logical qubits $L := \{q_0, q_1, \dots, q_{k-1}\}$ into $k+2$ physical qubits $T := D \cup A$, where $D = L$ and $A := \{q_X, q_Z\}$. The data register D stores the same quantum state as the logical qubit state of L , and the Iceberg code employs two redundant qubits A for encoding. The Iceberg code is classified as stabilizer code, and the code space is stabilized by $S_X = \otimes_{i \in T} X_i$ and $S_Z = \otimes_{i \in T} Z_i$. A syndrome measurement using two additional ancilla qubits can detect a single-qubit error. A k -bit string state $|x\rangle_L = |x_{k-1}\rangle \dots |x_1\rangle |x_0\rangle$ is encoded as

$$|x\rangle_L = \frac{|0\rangle_{q_Z} |f_x\rangle_{q_X} |x\rangle_D + |1\rangle_{q_Z} |\neg f_x\rangle_{q_X} |\neg x\rangle_D}{\sqrt{2}}, \quad (10)$$

where $\neg x$ is the logical not (negation) of x in the binary representation, $f_x = 0$ for even $\sum_{i=0}^{k-1} x_i$, and $f_x = 1$ for odd $\sum_{i=0}^{k-1} x_i$.

In the Iceberg code, the logical Pauli- X gates are defined as

$$\begin{aligned} \overline{X}_i &= X_{q_X} X_i \quad \forall i \in L \\ \overline{X}_i \overline{X}_j &= X_i X_j \quad \forall i, j \in L \\ \otimes_{j \in L \setminus i} \overline{X}_j &= X_{q_Z} X_i \quad \forall i \in L \\ \otimes_{j \in L} \overline{X}_j &= X_{q_X} X_{q_Z}, \end{aligned} \quad (11)$$

and the logical Pauli- Z gates are

$$\begin{aligned} \overline{Z}_i &= Z_{q_Z} Z_i \quad \forall i \in L \\ \overline{Z}_i \overline{Z}_j &= Z_i Z_j \quad \forall i, j \in L \\ \otimes_{j \in L \setminus i} \overline{Z}_j &= Z_{q_X} Z_i \quad \forall i \in L \\ \otimes_{j \in L} \overline{Z}_j &= Z_{q_X} Z_{q_Z}. \end{aligned} \quad (12)$$

Also, the logical Pauli- Y gates are given by

$$\begin{aligned} \overline{Y}_i \overline{Y}_j &= Y_i Y_j \quad \forall i, j \in L \\ \overline{X}_i \otimes_{j \in L \setminus i} \overline{Z}_j &= -Y_{q_X} Y_i \quad \forall i, j \in L \\ \overline{Z}_i \otimes_{j \in L \setminus i} \overline{X}_j &= -Y_{q_Z} Y_i \quad \forall i \in L \\ \otimes_{j \in L} \overline{Y}_j &= (-1)^{1+k/2} Y_{q_X} Y_{q_Z}. \end{aligned} \quad (13)$$

Here, the overline on an operator is used to clearly indicate that the operator is a logical gate.

A previous study [38] introduced the implementation method of logical rotation gates in a transversal manner using Mølmer-Sørensen (MS) gate [96]. The definition of the MS gate is

$$\text{MS}_{ij}(\theta) = \exp\left(-i\frac{\theta}{2} Z_i \otimes Z_j\right). \quad (14)$$

Logical rotation gates $\overline{R}_P(\theta) := e^{-i\frac{\theta}{2}\overline{P}}$ with respect to Pauli operators \overline{P} given by Eqs. (11), (12), and (13) can be implemented using an MS gate and a single-qubit gate for a basis transformation. For example, $\overline{R}_{XX}(\theta) = (H \otimes H)\text{MS}(\theta)(H \otimes H)$. Using the logical Pauli gates and logical rotation gates defined above, universal logical computation can be performed. Note that the encoding and syndrome measurements are performed in a fault-tolerant manner in the Iceberg code; however, the logical rotation gate is compiled into the physical gates set in a non-fault-tolerant manner.

3. Overall circuit

Although a recent study analyzed that the ITE method on a quantum computer was robust against quantum noise [97], the PITE method usually requires a large number of gate operations. Therefore, quantum devices that do not incorporate quantum error correction (QEC) are undesirable for the PITE method. As a first step, we consider the implementation of the Iceberg code [38]. The entire encoded quantum circuit for the PITE is depicted in Fig. 2. The quantum circuit used in this study consists of a total of eight qubits: six qubits for encoding a four-qubit system and two qubits for syndrome measurement. First, an encoding circuit is applied to generate a logical $|0\rangle_L$ state [38]. A single ancilla qubit is used as a flagged qubit to detect errors that occur during encoding [98]. In total, this involves seven two-qubit gate operations. Amplitude encoding is used to generate an encoded initial state $|\psi\rangle_L$ for PITE, where approximately 30 physical two-qubit gates are required for logical operations for amplitude encoding. Therefore, we performed syndrome measurements after amplitude encoding. Twelve two-qubit gates are required for the syndrome measurement. The PITE quantum circuit is then executed, as shown in Fig. 3. Because this quantum circuit involves many gate operations, a syndrome measurement is periodically performed within the block. Subsequently, by measuring the q_0 and q_Z quantum registers, the success state is obtained. The logical state is broken by measuring q_0 and q_Z registers. Thus, we reset the q_0 and q_Z registers and perform a re-encoding block to regenerate the encoded state. A detailed circuit diagram of the re-encoding block is presented in Fig. 4, where the flagged qubit is also used. The next PITE block is executed in the re-encoded state. This procedure is repeatedly applied until sufficient imaging time has elapsed. Finally, we performed destructive measurements of the remaining quantum registers.

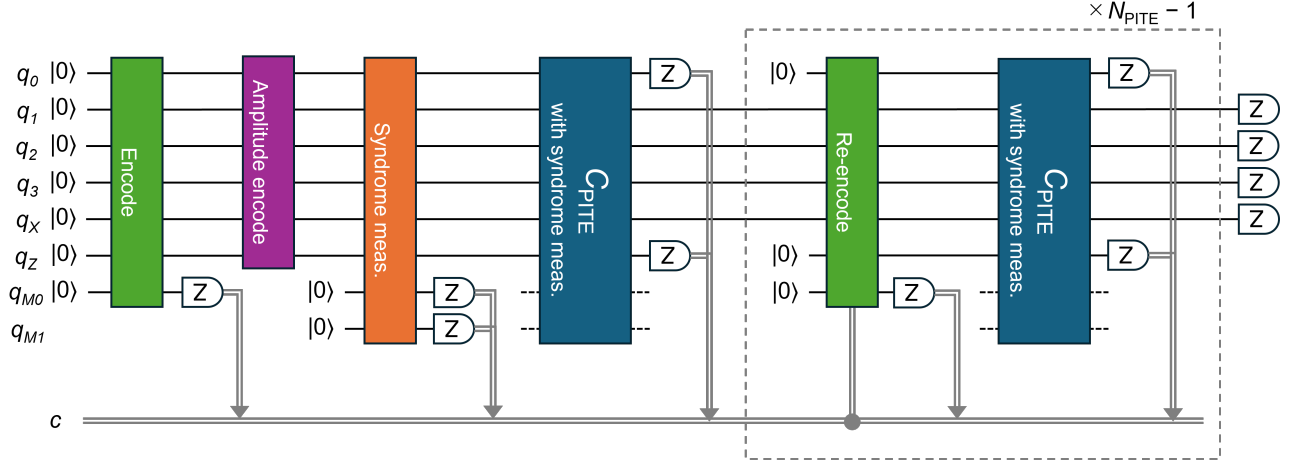


FIG. 2. The entire encoded quantum circuit for the PITE comprises eight quantum registers $\{q_i\}$ and classical registers c . The measurement results with respect to Z basis are stored in the classical registers c (gray lines with arrows). The encoded circuit generates $|0\rangle_L$ in code space. The amplitude-encoding circuit is operated to prepare an initial state for the PITE, which contains approximately thirty two-qubit gates. Subsequently, the syndrome measurement is applied. After preparing the encoded initial state, the first step of the PITE is performed, including several syndrome measurements that act at almost equal intervals. Then, q_0 and q_z registers are observed to collapse the entangled state to the success state. After measuring q_0 and q_z registers, the re-encode circuit is applied to recover the encoded state, which contains conditional operations based on classical registers. Re-encoding circuits, PITE circuits with syndrome measurement, Z -basis measurement are repeatedly performed until sufficient imaginary-time has elapsed.

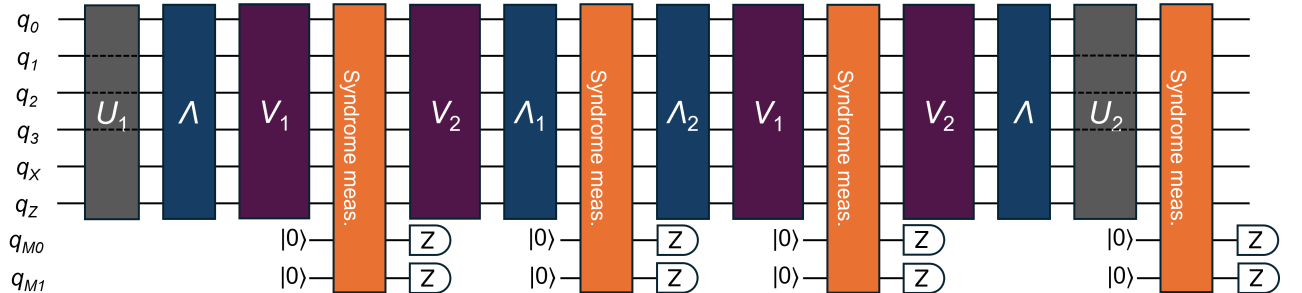


FIG. 3. The detailed circuit diagram of PITE including syndrome measurements in Figure 2. U_1 and U_2 denote the logical single-qubit gates on the ancilla qubit of PITE. Other blocks, excluding the syndrome measurement, are logical RTE operators, and the generators are indicated in these blocks.

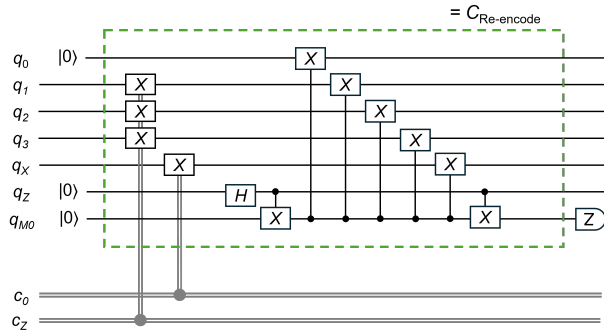


FIG. 4. Detailed circuit diagram of the re-encoding block $C_{\text{Re-encode}}$ of the quantum circuit shown in Figure 2. Classical registers c_0 and c_Z store the measurement results of quantum registers q_0 and q_z , respectively.

4. PITE in encoded state

The logical amplitude encoding is implemented by decomposing it into native gates of the Iceberg code such as $\{R_X, R_Z, R_{XX}, R_{YY}, R_{ZZ}\}$. However, to optimize the number of gate operations, we consider a detailed implementation of the CRTE gate, which is the main building block of our algorithm. The main feature of the Iceberg code is that it can efficiently implement global rotations that act on the entire logical space. The forward- and backward-CRTE gates in the approximated PITE circuit are rewritten as

$$e^{-is\Delta\tau\mathcal{H}} \otimes |0\rangle\langle 0| + e^{is\Delta\tau\mathcal{H}} \otimes |1\rangle\langle 1| = e^{-is\Delta\tau\mathcal{H}\otimes Z}. \quad (15)$$

As shown in Eq. (8), because the Hamiltonian is expressed as a linear combination of Pauli operators, the

CRTE operator can be decomposed into a sequence of rotation gates using Trotter-Suzuki decomposition [99]. Let us now consider an efficient implementation. First, we decompose the generator of the CRTE operators as

$$\mathcal{H} \otimes Z = \Lambda + V, \quad (16)$$

where Λ denotes the diagonal part and V is the non-diagonal part of the generator. Importantly, the computational model in this study comprises of the larger values of diagonal coefficients for Λ and smaller values of non-diagonal coefficients for V . This is often the case with quantum chemistry, because you usually start from a good mean-field Hamiltonian such as DFT or Hartree-Fock to include the electron correlation. We would like to stress here that by introducing such a decomposition, we can implement $\Lambda + V$ efficiently, as follows. We used the second-order Trotter-Suzuki decomposition as:

$$e^{-it(\Lambda+V)} = \left[e^{-i\frac{t}{2r}\Lambda} e^{-i\frac{t}{r}V} e^{-i\frac{t}{2r}\Lambda} \right]^r + O\left(\left(\frac{t}{r}\right)^3\right). \quad (17)$$

Note that we can implement the RTE of Λ exactly. The first-order Trotter-Suzuki decomposition is sufficient to implement the RTE for V composed of the small coefficients of the Pauli operators. We remark that the second-order Trotter decomposition can be implemented only for the additional cost of $e^{it\Lambda/(2r)}$ to the first-order Trotter decomposition. Figure 3 shows a detailed schematic of the PITE circuit when the dividing number of the CRTE gate is $r = 2$. The quantum circuit was implemented by decomposing it as $\Lambda = \Lambda_1 + \Lambda_2$ and $V = V_1 + V_2$, so that the syndrome measurement is inserted after every interval of approximately 40 quantum gate operations. The specific expression of Eq. (16) used in this study is given in the appendix C.

The input state for the PITE is prepared for the quantum register $L_S := \{q_1, q_2, q_3\}$. The encoded initial state $|\psi\rangle_{L_S}|0\rangle_{q_0}$ is changed by applying PITE operator as,

$$\sum_{k=0}^{N-1} \left(c_k^{(\text{succ})} |k\rangle_{L_S} |0\rangle_{q_0} + c_k^{(\text{fail})} |k\rangle_{L_S} |1\rangle_{q_0} \right), \quad (18)$$

where $N = 2^n$, and $c_k^{(\text{succ})}$ and $c_k^{(\text{fail})}$ represent the expansion coefficients of the success and failure states with respect to the computational basis, respectively. In the Iceberg code, the state acted on by the ITE operator is represented by the physical qubits as

$$\begin{aligned} & \sum_{k=0}^{N-1} c_k^{(\text{succ})} \frac{|0\rangle_{q_Z} |f_k\rangle_{q_X} |k\rangle_{D_S} |0\rangle_{q_0} + |1\rangle_{q_Z} |\neg f_k\rangle_{q_X} |\neg k\rangle_{D_S} |1\rangle_{q_0}}{\sqrt{2}} \\ & + c_k^{(\text{fail})} \frac{|0\rangle_{q_Z} |\neg f_k\rangle_{q_X} |k\rangle_{D_S} |1\rangle_{q_0} + |1\rangle_{q_Z} |f_k\rangle_{q_X} |\neg k\rangle_{D_S} |0\rangle_{q_0}}{\sqrt{2}}. \end{aligned} \quad (19)$$

Measuring q_0 and q_Z collapses the entangled state to the success state:

$$\frac{1}{\sqrt{p_{\text{succ}}}} \sum_{k=0}^{N-1} c_k^{(\text{succ})} \frac{|f_k\rangle_{q_X} |k\rangle_{D_S}}{\sqrt{2}}, \quad (20)$$

when observing the physical qubits as $|0\rangle_{q_Z} |0\rangle_{q_0}$ state and

$$\frac{1}{\sqrt{p_{\text{succ}}}} \sum_{k=0}^{N-1} c_k^{(\text{succ})} \frac{|\neg f_k\rangle_{q_X} |\neg k\rangle_{D_S}}{\sqrt{2}}, \quad (21)$$

for the physical qubit state being $|1\rangle_{q_Z} |1\rangle_{q_0}$ state. Here, p_{succ} is the success probability, where the encoded ancilla qubit of the PITE circuit is observed as $|0\rangle_{q_0}$ state. In contrast, observing the unencoded qubits as $|0\rangle_{q_Z} |1\rangle_{q_0}$ and $|1\rangle_{q_Z} |0\rangle_{q_0}$ corresponds to the failure state. If the ancilla qubit of q_Z is measured as $|0\rangle_{q_Z}$ state, we operate X gates on the system qubits. In addition, if the ancilla qubit of q_0 is measured as $|0\rangle_{q_0}$ state, we act X gate on the ancilla qubit of q_X . By applying such conditional- X gates with respect to classical registers, we have the unencoded states as

$$\sum_{k=0}^{N-1} \tilde{c}_k^{(\text{succ})} |0\rangle_{q_Z} |f_k\rangle_{q_X} |k\rangle_{D_S} |0\rangle_{q_0} \quad (22)$$

for success state and

$$\sum_{k=0}^{N-1} \tilde{c}_k^{(\text{fail})} |0\rangle_{q_Z} |f_k\rangle_{q_X} |k\rangle_{D_S} |0\rangle_{q_0} \quad (23)$$

for failure state, where we reset the measured qubits of q_0 and q_Z and $\tilde{c}_k^{(\text{succ})} = c_k^{(\text{succ})} / \sqrt{p_{\text{succ}}}$. The gate operations are shown in Fig. 4 leads to the encoded state:

$$\begin{aligned} & \sum_{k=0}^{N-1} \tilde{c}_k^{(\text{succ})} \frac{|0\rangle_{q_Z} |f_k\rangle_{q_X} |k\rangle_{D_S} |0\rangle_{q_0} + |1\rangle_{q_Z} |\neg f_k\rangle_{q_X} |\neg k\rangle_{D_S} |1\rangle_{q_0}}{\sqrt{2}} \\ & = \sum_{k=0}^{N-1} \tilde{c}_k^{(\text{succ})} |k\rangle_{L_S} |0\rangle_{q_0}. \end{aligned} \quad (24)$$

With the same manner as the encoded success state, the encoded failure state $\sum_{k=0}^{N-1} \tilde{c}_k^{(\text{fail})} |k\rangle_{L_S} |0\rangle_{q_0}$ is obtained using the re-encoding circuit shown in Fig. 4.

III. RESULTS

A. Classical computation

1. NV center in diamond

The accuracy of the treatment of spin defects is verified by performing exact diagonalization (FCI calculation) of the derived low-energy effective model on a classical computer before quantum calculations are performed. First, calculations are performed on NV⁻-center in diamond, which are often applied to high-accuracy calculation methods for spin defects. Figure 5(a) shows the spin density of the defect level obtained from the DFT calculations without spin restrictions. Figure 5(b) shows the KS defect levels obtained from spin-restricted DFT calculations. This confirms that defect levels existed between

the conduction and valence bands. The active space was set to include only the energy levels of gap states. It can be seen that the spin density with C_{3v} symmetry is formed by the dangling bonds around the carbon vacancy directly above the [111] direction of the nitrogen atom, which results in the degeneracy of e_x and e_y orbitals in the KS defect levels.

The results of diagonalizing the low-energy effective model, which incorporates the effects of bands outside the active space as screening effects, are shown in Fig. 5(c). This correctly reproduces the order of excited states, such as $^3A_2 < ^1E < ^1A_1 < ^3E$. The eigenvectors of the effective Hamiltonian are summarized in Table II. By checking each spin state, 3A_2 and 3E states correspond to spin triplet states, and 1E and 1A_1 state correspond to spin singlet states. As is well known, looking at the Table II, spin triplet states are described by single-Slater determinants. In contrast, spin singlet states in nature require a multiplicity of Slater determinants. The eigenvalues were consistent with those of previous theoretical and experimental studies. In a previous study [100] which created an effective model at the level of cRPA, the excitation energy was 0.47/1.36/2.05 eV for $^1E/{}^1A_1/{}^3E$ states, which is in good agreement with the results of this study, which are summarized in Table I. Ma et al. applied density matrix embedding theory (DMET) [101–103] that incorporates an exchange-correlation effect beyond the RPA approximation to the spin defects, and reported that it shows good agreement with experimental values as 0.56/1.76/2.00 eV for ${}^1E/{}^1A_1/{}^3E$ states [104–106]. A comparison of the computational methods proposed thus far for calculating the excited states in NV[−] center diamonds with the results of this study is summarized in Appendix B.

TABLE I. Computed vertical excitation energies (eV) of NV[−]-center in diamond.

Excitation	This work	Expt.
${}^3A_2 \rightarrow {}^3E$	2.11	1.945 [107]
${}^3A_2 \rightarrow {}^1A_1$	1.46	
${}^3A_2 \rightarrow {}^1E$	0.64	
${}^1E \rightarrow {}^1A_1$	0.82	1.190 [108]
${}^1A_1 \rightarrow {}^3E$	0.66	≈ 0.4 [109]

2. Complex defects in w-AlN

Previous studies [64, 65] calculated the defect formation energy of charged point defects in a crystal of w-AlN using the finite-size correction of Freysoldt, Neugebauer, and Van de Walle (FNV) [110]. They concluded that complex defects, such as $(\text{Zr}_{\text{Al}}\text{V}_\text{N})^0$, $(\text{Ti}_{\text{Al}}\text{V}_\text{N})^0$, and $(\text{Hf}_{\text{Al}}\text{V}_\text{N})^0$ can be produced. The results for the three complex defects are similar to each other. Thus, in

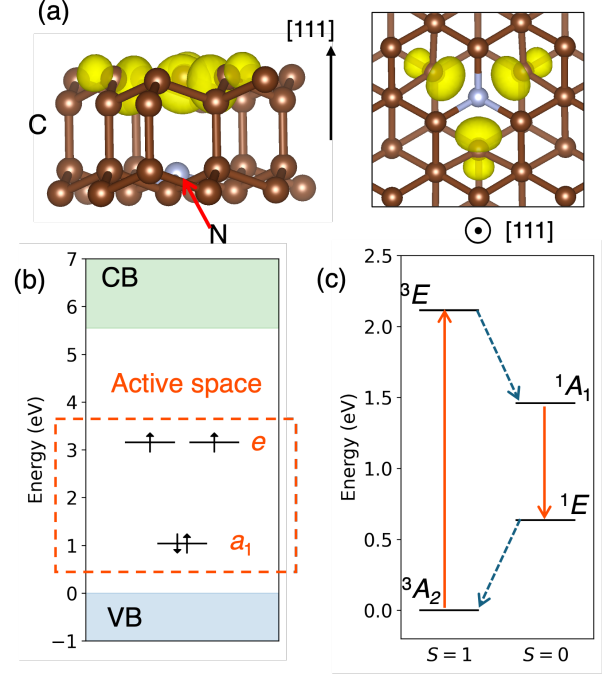


FIG. 5. The electronic structure of NV[−] in diamond was computed on a classical computer. (a) Spin densities obtained from spin-unrestricted DFT calculations. Isosurfaces are displayed at 10% of the maximum value. (b) Single-particle defect levels obtained by spin-restricted DFT calculations. The orange dashed box denotes the energy region to be considered for constructing a low-energy effective Hamiltonian. (c) Excitation energies calculated using exact diagonalization (FCI calculations).

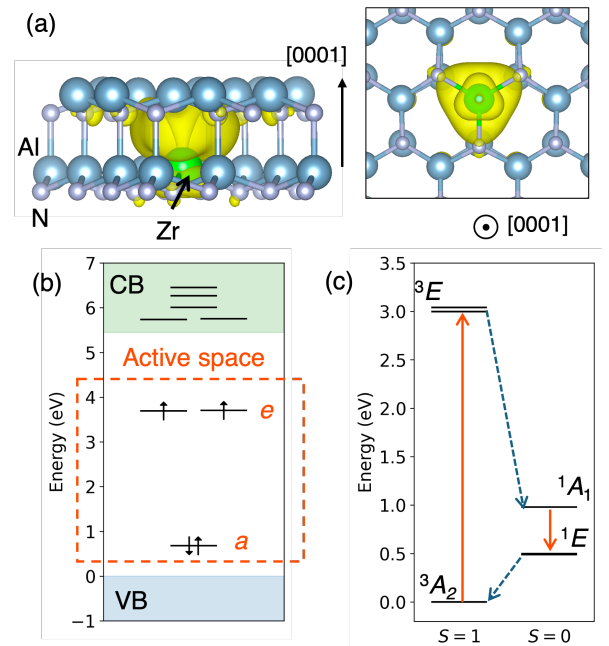


FIG. 6. Same as Figure 5 for $(\text{Zr}_{\text{Al}}\text{V}_\text{N})^0$ in w-AlN.

TABLE II. Computed many-body wave function of NV^- -center in diamond.

State	Many-body wave function
3E	$ e_y\uparrow e_y\downarrow e_x\uparrow a_1\uparrow\rangle, e_y\uparrow e_y\downarrow e_x\downarrow a_1\downarrow\rangle, 0.71(e_y\uparrow e_y\downarrow e_x\downarrow a_1\uparrow\rangle + e_y\uparrow e_y\downarrow e_x\uparrow a_1\downarrow\rangle), e_y\uparrow e_x\uparrow e_x\downarrow a_1\uparrow\rangle, e_y\downarrow e_x\uparrow e_x\downarrow a_1\downarrow\rangle, 0.71(e_y\downarrow e_x\uparrow e_x\downarrow a_1\uparrow\rangle + e_y\uparrow e_x\uparrow e_x\downarrow a_1\downarrow\rangle)$
1A_1	$0.68(e_x\uparrow e_x\downarrow a_1\uparrow a_1\downarrow\rangle + e_y\uparrow e_y\downarrow a_1\uparrow a_1\downarrow\rangle) - 0.26 e_y\uparrow e_y\downarrow e_x\uparrow e_x\downarrow\rangle$
1E	$0.51(e_y\uparrow e_x\downarrow a_1\uparrow a_1\downarrow\rangle - e_y\downarrow e_x\uparrow a_1\uparrow a_1\downarrow\rangle) + 0.19(e_y\uparrow e_y\downarrow e_x\downarrow a_1\uparrow\rangle - e_y\uparrow e_y\downarrow e_x\uparrow a_1\downarrow\rangle) - 0.45(e_x\uparrow e_x\downarrow a_1\uparrow a_1\downarrow\rangle - e_y\uparrow e_y\downarrow a_1\uparrow a_1\downarrow\rangle), 0.51(e_x\uparrow e_x\downarrow a_1\uparrow a_1\downarrow\rangle - e_y\uparrow e_y\downarrow a_1\uparrow a_1\downarrow\rangle) + 0.19(e_y\downarrow e_x\uparrow e_x\downarrow a_1\uparrow\rangle - e_y\uparrow e_x\uparrow e_x\downarrow a_1\downarrow\rangle) - 0.45(e_y\uparrow e_x\downarrow a_1\uparrow a_1\downarrow\rangle - e_y\downarrow e_x\uparrow a_1\uparrow a_1\downarrow\rangle)$
3A_2	$ e_y\uparrow e_x\uparrow a_1\uparrow a_1\downarrow\rangle, e_y\downarrow e_x\downarrow a_1\uparrow a_1\downarrow\rangle, 0.71(e_y\uparrow e_x\downarrow a_1\uparrow a_1\downarrow\rangle + e_y\downarrow e_x\uparrow a_1\uparrow a_1\downarrow\rangle)$

the main text, we explain the results based mainly on $(\text{Zr}_{\text{Al}}\text{V}_\text{N})^0$. See the other two complex defects in the Appendix. D.

Figure 6 presents the classical computational results for the $(\text{Zr}_{\text{Al}}\text{V}_\text{N})^0$ complex in w-AlN. Fig. 6(a) presents the spin density obtained from spin-unrestricted DFT calculation. The spin density of the $(\text{Zr}_{\text{Al}}\text{V}_\text{N})^0$ complex exhibits dangling bonds of the Zr atom spreading around the nitrogen defect while holding the C_{3v} symmetry. The KS defect levels calculated by spin-restricted DFT calculations were located within the band gap, as shown in Fig. 6(b). The defect level diagram of the $(\text{Zr}_{\text{Al}}\text{V}_\text{N})^0$ complex exhibits the same structure as the NV^- -center in diamond. In addition to the a_1 , e_x and e_y orbitals, $(\text{Zr}_{\text{Al}}\text{V}_\text{N})^0$ complex in w-AlN also has defect levels arising from Zr atoms that appear near the conduction band minimum (CBM). The average value of the transfer integral between the Wannier orbitals ($t = 1.01$ eV) is sufficiently small compared with the energy difference from the e orbital to the CBM. Therefore, the effect of the coupling between the e orbitals and CBM is small, and the defect level can be considered isolated within the band gap. Therefore, we adopted an active space that included the a_1 and e orbitals.

The results of the calculations for the low-energy effective model are shown in Figure 6(c). Theoretical calculations predict that the order of the energy levels will be the same as that in the NV case, although the quantitative values will differ. Unlike the NV^- -center in diamond, a small split of around 0.04 and 0.01 eV occurs in the 3E and 1E states, respectively. After checking the wavefunction and symmetry, we concluded that this was because of the finite cell size. In the 96-atom supercell calculation, the splitting of the e_x and e_y KS defect levels increases, resulting in a larger split in the 3E and 1E states. Table III summarizes the many-body wave function states obtained from FCI calculations. It is composed of multiple Slater determinants, which indicates that DFT calculations is difficult to describe the singlet states of $(\text{Zr}_{\text{Al}}\text{V}_\text{N})^0$ complex in w-AlN. The excited energies for other vacancy complexes are summarized in Appendix D, where the calculation settings are the same as $(\text{Zr}_{\text{Al}}\text{V}_\text{N})^0$ complex.

TABLE III. Computed many-body wave function of the ZrV in w-AlN.

State	Many-body wave function
3E	$ e_y\uparrow e_y\downarrow e_x\uparrow a_1\uparrow\rangle, e_y\uparrow e_y\downarrow e_x\downarrow a_1\downarrow\rangle, e_y\uparrow e_x\uparrow e_x\downarrow a_1\uparrow\rangle, e_y\downarrow e_x\uparrow e_x\downarrow a_1\downarrow\rangle, 0.71(e_y\uparrow e_y\downarrow e_x\downarrow a_1\uparrow\rangle + e_y\uparrow e_y\downarrow e_x\uparrow a_1\downarrow\rangle), 0.71(e_y\downarrow e_x\uparrow e_x\downarrow a_1\uparrow\rangle + e_y\uparrow e_x\uparrow e_x\downarrow a_1\downarrow\rangle)$
1A_1	$0.64 e_x\uparrow e_x\downarrow a_1\uparrow a_1\downarrow\rangle - 0.77 e_y\uparrow e_y\downarrow a_1\uparrow a_1\downarrow\rangle$
1E	$0.71(e_y\uparrow e_x\downarrow a_1\uparrow a_1\downarrow\rangle - e_y\downarrow e_x\uparrow a_1\uparrow a_1\downarrow\rangle), 0.77 e_x\uparrow e_x\downarrow a_1\uparrow a_1\downarrow\rangle - 0.64 e_y\uparrow e_y\downarrow a_1\uparrow a_1\downarrow\rangle$
3A_2	$ e_y\uparrow e_x\uparrow a_1\uparrow a_1\downarrow\rangle, e_y\downarrow e_x\downarrow a_1\uparrow a_1\downarrow\rangle, 0.71(e_y\uparrow e_x\downarrow a_1\uparrow a_1\downarrow\rangle + e_y\downarrow e_x\uparrow a_1\uparrow a_1\downarrow\rangle)$

B. Quantum computation of the spin defects

1. Setup

The quantum circuits were constructed using `qiskit` v1.1.0 [111], where the mapping of the fermionic Hamiltonian to spin operators was performed with `qiskit-nature` v0.7.2. We then translated it into the quantum circuit of `pytket` with `pytket` v1.28.0 [112] and `pytket-qiskit` v0.53.0, and executed the quantum circuit with `pytket-quantinuum` v0.33.0. We used the Quantinuum H1-1 trapped-ion computer and its emulator (H1-1E) [38, 68]. The H1-1 quantum computer is composed of 20 qubits and can perform MS gate operations combined with all-to-all connectivity of $\sim 2.0 \times 10^{-3}$ infidelity [113]. We ran 1000 shots of quantum computation.

In this study, we calculated the ground and excited states of the singlet state of $(\text{Zr}_{\text{Al}}\text{V}_\text{N})^0$ in w-AlN. This state is composed of multiple Slater determinants, as shown in Table III; therefore, the DFT calculation fails to describe the ground and excited states of the spin singlet state. When performing quantum calculations, we ignored terms whose absolute value of the Hamiltonian coefficient was less than 0.01. This approximation resulted in finding the \mathbb{Z}_2 symmetry for the $P_{Z_2} = ZIZI$ operator, that is, the Hamiltonian is commutative with

the P_{Z_2} operator [91]. This symmetry allows for the reduction of the number of qubits by one, and the total number of logical qubits, including an ancilla qubit of PITE, becomes four, which can be implemented in the quantum circuit in Figure 2. In addition, the effect of the approximation is not observed at the second decimal point.

2. Ground state of the singlet state

In this study, we prepared a good initial state for PITE as $|\psi\rangle = (3|\phi_{\text{gs}}\rangle + |\phi_{\text{es1}}\rangle + |\phi_{\text{es2}}\rangle + |\phi_{\text{es3}}\rangle)/\sqrt{12}$, owing to hardware limitation. The drawback of the original PITE method is that the total success probability exponentially decreases with respect to m_0 as the number of PITE steps increases [114]. To avoid this drawback, a constant energy shift was used [114]. Note that a constant energy shift requires ground-state energy, and the approximated ITE operator in Eq. (9) will be the cosine operators, $\cos(\Delta E_k \Delta \tau s_1)$, where the approximated PITE circuit is related to cosine filtering [115] and Rodeo's algorithm [116] except for parameter choice. In a constant energy shift, the total success probability becomes $P_0 = |c_1|^2$. The details of the computational cost of the PITE method were analyzed in [114]. We performed four steps of the PITE operations. We linearly changed $\Delta \tau_k$ from 0.25 to $\pi/[2s_1(E_{\text{es1}} - E_{\text{gs}})] = 2.41$, where $m_0 = 0.8$. Because the accuracy of the Trotter-Suzuki decomposition for CRTE gates worsens as $\Delta \tau_k$ increases, the dividing numbers for $\Delta \tau_k$ are chosen as $r = (1, 2, 3, 4)$. At each step of the PITE, the number of syndrome measurements performed is (2, 4, 6, 8), and the number of two-qubit gate operations, including the syndrome measurement, is (92, 178, 257, 336). A total of 21 syndrome measurements were performed.

Figure 7(a) shows the results of the discard rate obtained by the QED. The quantum error of H1-1 quantum computer is modeled as depolarizing error and a fitting function of the discard rate is given by [95]

$$d(N_{2Q}, p_2) = 1 - (1 - p_2)^{N_{2Q}}, \quad (25)$$

where N_{2Q} denotes the number of two-quantum gates within the circuit. We adopted the fitting parameter $p_2 = 1.6 \times 10^{-3}$ used in a previous experiment [95] and confirmed that it also agrees well with our experiment. It is clearly seen that the discard rates of H1-1 and H1-1E agree well with each other, confirming that the quantum noise that occurs on the actual device can be well modeled by the emulator.

The total success probability for the PITE steps is presented in 7(b). In the PITE with an energy shift, the total success probability approaches the overlap between the initial and ground states. The quantum noise-free calculation result gives a value of 0.78, which is slightly larger than the overlap of 0.75, but this is confirmed to be due to the error in the Trotter-Suzuki decomposition.

A reduction in the total success probability was observed in cases without QED.

The measured probabilities of each Slater determinant, that is, the absolute square of the coefficients of the Slater determinant, are shown in Figure 7(c). There is a slight deviation between the results of the FCI calculation and the noiseless simulation of the PITE for the effective Hamiltonian. This deviation is due to the error of the Trotter-Suzuki decomposition and finite number of measurements. In the histogram in Figure 7(c), H1-1 and H1-1E are in good agreement, as in the case of total success probability. In both results, a slight amplitude was observed in states other than $|e_{x\uparrow}e_{x\downarrow}a_{1\uparrow}a_{1\downarrow}\rangle$ and $|e_{y\uparrow}e_{y\downarrow}a_{1\uparrow}a_{1\downarrow}\rangle$. This is considered to be due to the influence of quantum errors that are not detected by the QED, such as two-qubit errors. We quantify the results using classical fidelity [117] defined as

$$F(|\Psi^{\text{FCI}}\rangle, |\Psi\rangle) := \left(\sum_i |c_i^{\text{FCI}}||c_i^\beta| \right)^2, \quad (26)$$

where $|\Psi^{\text{FCI}}\rangle = \sum_i c_i |i\rangle$ represents the ground state obtained by FCI calculation and $|\Psi\rangle$ is ground state by PITE. The classical fidelity of H1-1 with QED is 0.98, and we can observe that the results have improved compared with the classical fidelity of 0.87, which does not use QED. We note that the unencoded circuit contains 743 two-qubit gates. As a result, this experiment indicates that the influence of quantum errors that are not detected by the QED is small, and the ground state of the singlet state is successfully obtained in a trapped-ion quantum computer.

The calculation results using the emulator for Quantinuum H1-1 for NV⁻ center in diamond, and (Hf_{Al}V_N)⁰ and (Ti_{Al}V_N)⁰ complexes in w-AlN are summarized in Appendix D.

3. Excited state of spin singlet

Using a filter circuit [118, 119] which removes states with a given eigenvalue, the excited state can be obtained. However, a filter circuit must also be implemented in addition to the quantum circuit used to obtain the ground state; therefore, it is difficult to execute the excited-state calculation on current quantum hardware limited by the number of gate operations. In this study, we assume that the ground state has been obtained using techniques such as quantum tomography, and we use the initial state after removing the ground state.

In the calculation, the initial state is prepared as $|\psi\rangle = (|\phi_{\text{es1}}\rangle + |\phi_{\text{es2}}\rangle + |\phi_{\text{es3}}\rangle)/\sqrt{3}$. We performed four steps of the PITE operations. We linearly changed $\Delta \tau_k$ from 0.05 to $\pi/[2s_1(E_{\text{es2}} - E_{\text{es1}})] = 0.57$, where $m_0 = 0.8$. As $\max \Delta \tau_k$ is smaller than that of the ground-state calculation, the dividing numbers for $\Delta \tau_k$ are $r = (1, 1, 2, 3)$. Fifteen syndrome measurements were used for the calculations. The encoded and unencoded quantum circuits

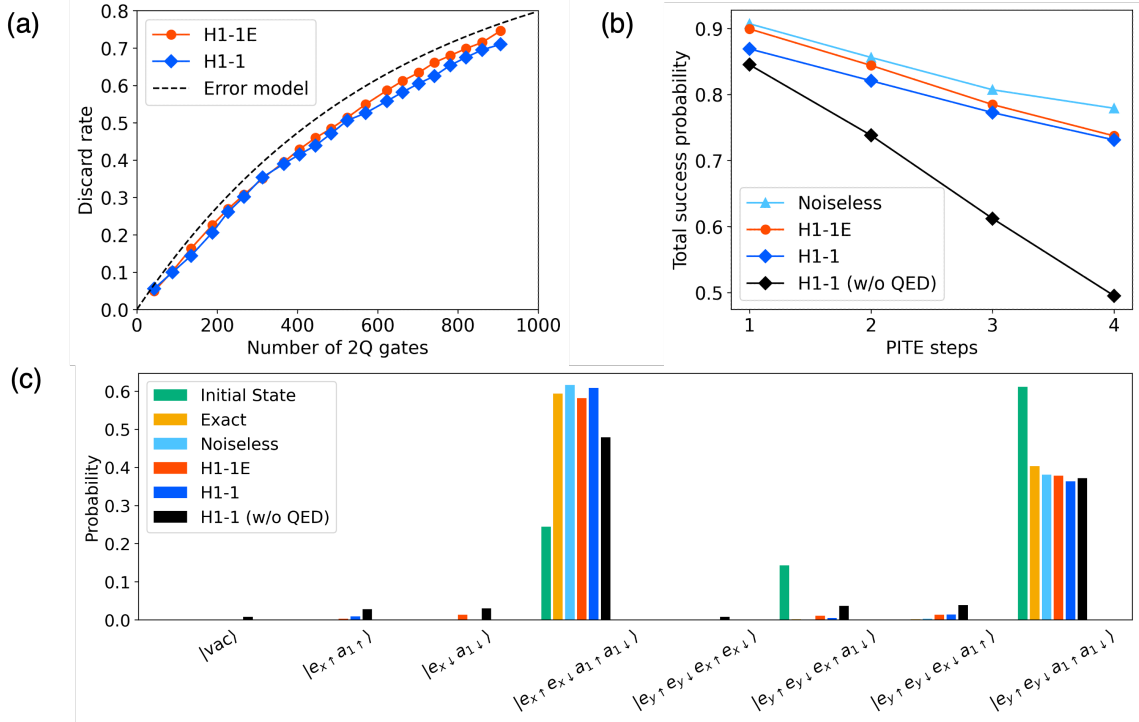


FIG. 7. Computation results for $(\text{ZrAlV}_N)^0$ complex in w-AlN obtained using a quantum computer. (a) Discard rates of the calculated results owing to errors detected by QED as a function of the number of two-qubit gates. The dashed line denotes the noise model shown in Eq. (25), with $p_2 = 1.6 \times 10^{-3}$. (b) Total success probability of PITE according to the PITE steps. (c) Histogram of measured computational basis. Noiseless denotes the noiseless simulation of the PITE, and H1-1E denotes the emulator of the H1-1 quantum computer. All calculations used $N_{\text{shot}} = 1000$.

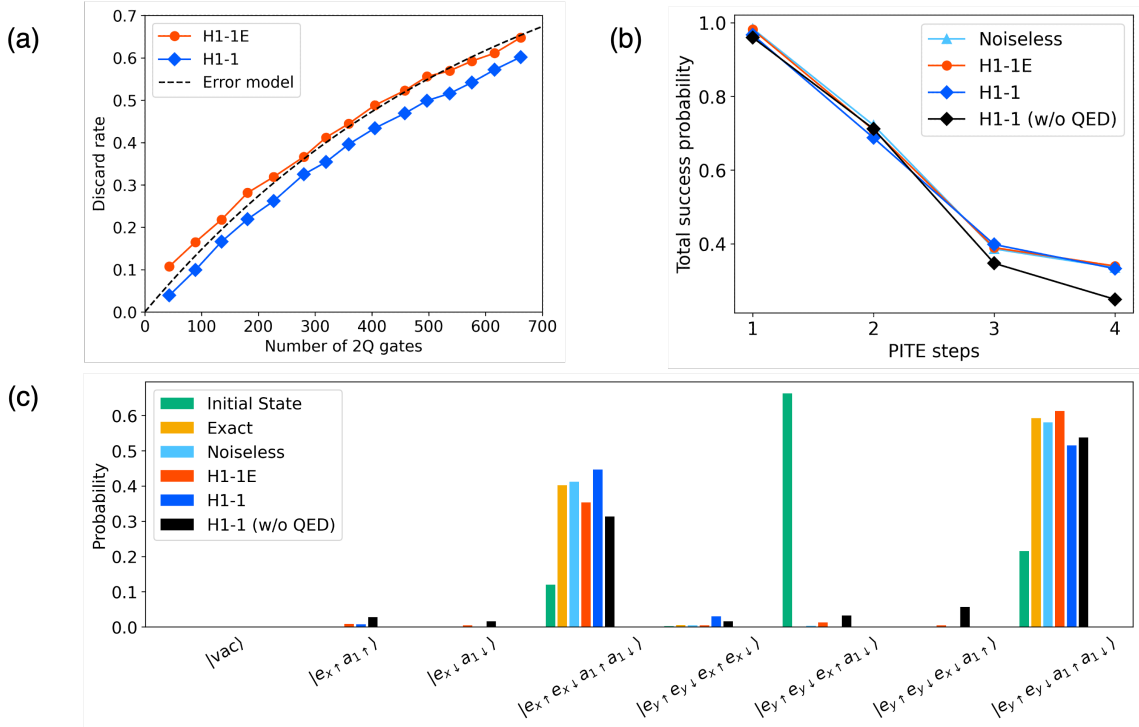


FIG. 8. Same as Figure 7 for the excited state.

contained 662 and 537 two-qubit gate operations, respectively.

As with the ground-state calculation, the discard rate is shown in Fig. 8(a). The discard rate for H1-1 is 0.60, and that for H1-1E is 0.65. H1-1 has slightly less quantum noise than H1-1E; however, both are consistent with the fitting of the noise model in Eq. (25).

The total success probability for the PITE is shown in Fig. 8(b). The results of the noiseless simulation and encoded simulation (H1-1 and H1-1E) show similar values, but it was observed that the total success probability is smaller in the case without QED. The measured probability of Slater determinants is presented in Fig. 8(c). It can be confirmed that the classical fidelities of H1-1 and H1-1E using QED are 0.98 and 0.97, respectively, and that QED improves on the classical fidelity of 0.87 which does not use QED.

IV. CONCLUSIONS

A low-energy effective model for calculating the electronic state of a quantum spin was constructed, and the probabilistic imaginary-time evolution (PITE) algorithm, designed for the fault-tolerant quantum computer (FTQC) era, was applied to the effective Hamiltonian in order to calculate the ground state and excited states of the singlet state on a Quantinuum trapped-ion quantum computer. In order to address the quantum noise that occurs in quantum hardware, the PITE method was implemented using the $\llbracket n+2, n, 2 \rrbracket$ quantum error detection (QED) code, referred to as the Iceberg code. The Quantinuum hardware facilitates mid-circuit measurements and reuse, which is advantageous for QED syndrome measurements and ancilla-qubit measurements in PITE. In quantum computation with an encoded state, it is essential to measure the ancilla qubit of PITE at each PITE step. However, this measurement results in the destruction of the encoded state. To address this challenge, we employed re-encoding to recover the encoded state. Furthermore, we concentrated on the fact that the low-energy effective Hamiltonian can be divided into a large diagonal term resulting from the one-body term and a small non-diagonal term based on the two-body interaction. We also developed a circuit implementation that reduces the number of two-qubit gates based

on second-order Trotter-Suzuki decomposition.

An effective low-energy model has been constructed for the NV centre in diamond, which is a promising quantum sensing material, and for complex defects in w-AlN, which is expected to be a new spin-qubit material. The constructed effective Hamiltonian was confirmed to correctly describe the energy order of the excitation energies. We performed calculations of the ground and excited states of $\text{Zr}_{\text{Al}}\text{V}_\text{N}$ complex in w-AlN using the Quantinuum H1-1 quantum computer. The quantum circuit for PITE with QED included up to 906 two-qubit gates, with a discard rate of 71% due to the QED. The implementation of QED confirmed that the ground and excited states can be obtained with a classical fidelity of 0.98.

In this study, the simulation results were discarded when quantum errors were detected using QED. However, this resulted in an increase in the variance of finite measurements. Therefore, it would be beneficial to implement quantum error correction. Furthermore, due to the constraints of the hardware, the minimum active space, comprising the a and e orbitals, was selected for the calculations. However, it would be more optimal to utilise a broader active space to enhance the precision of the calculations. As the number of orbitals included in the active space increases, the computational complexity rises exponentially, rendering classical computers inadequate for such calculations. Consequently, the potential of quantum computers is expected to expand considerably [120]. As PITE has already been demonstrated to be quadratically accelerated [66], it may be possible in the future to provide experimental evidence that quantum computation is more effective than classical computation in practical calculations based on advances in hardware.

ACKNOWLEDGMENTS

The author acknowledges the contributions and discussions provided by the members of Quemix Inc. The authors thank the Supercomputer Center, the Institute for Solid State Physics, the University of Tokyo for the use of the facilities. This work was supported by JSPS KAKENHI under Grant-in-Aid for Scientific Research No.21H04553, No.20H00340, and No.22H01517, JSPS KAKENHI. This work was partially supported by the Center of Innovations for Sustainable Quantum AI (JST Grant Number JPMJPF2221).

[1] S. Lloyd, Universal quantum simulators, *Science* **273**, 1073 (1996), <https://www.science.org/doi/pdf/10.1126/science.273.5278.1073>. <https://www.pnas.org/doi/10.1073/pnas.0808245105>.

[2] D. S. Abrams and S. Lloyd, Simulation of many-body fermi systems on a universal quantum computer, *Phys. Rev. Lett.* **79**, 2586 (1997).

[3] I. Kassal, S. P. Jordan, P. J. Love, M. Mohseni, and A. Aspuru-Guzik, Polynomial-time quantum algorithm for the simulation of chemical dynamics, *Proceedings of the National Academy of Sciences* **105**, 18681 (2008), <https://www.pnas.org/doi/10.1073/pnas.0808245105>.

[4] A. M. Childs and N. Wiebe, Hamiltonian simulation using linear combinations of unitary operations, *Quantum Info. Comput.* **12**, 901–924 (2012).

[5] D. W. Berry, A. M. Childs, R. Cleve, R. Kothari, and R. D. Somma, Simulating hamiltonian dynamics with

a truncated taylor series, *Phys. Rev. Lett.* **114**, 090502 (2015).

[6] G. H. Low and I. L. Chuang, Hamiltonian simulation by qubitization, *Quantum* **3**, 163 (2019).

[7] A. M. Childs, Y. Su, M. C. Tran, N. Wiebe, and S. Zhu, Theory of trotter error with commutator scaling, *Phys. Rev. X* **11**, 011020 (2021).

[8] A. Y. Kitaev, Quantum measurements and the Abelian Stabilizer Problem, *arXiv e-prints*, quant-ph/9511026 (1995), arXiv:quant-ph/9511026 [quant-ph].

[9] D. S. Abrams and S. Lloyd, Quantum algorithm providing exponential speed increase for finding eigenvalues and eigenvectors, *Phys. Rev. Lett.* **83**, 5162 (1999).

[10] Z. Ding and L. Lin, Simultaneous estimation of multiple eigenvalues with short-depth quantum circuit on early fault-tolerant quantum computers, *Quantum* **7**, 1136 (2023).

[11] Z. Ding and L. Lin, Even shorter quantum circuit for phase estimation on early fault-tolerant quantum computers with applications to ground-state energy estimation, *PRX Quantum* **4**, 020331 (2023).

[12] T. Kadowaki and H. Nishimori, Quantum annealing in the transverse ising model, *Phys. Rev. E* **58**, 5355 (1998).

[13] E. Farhi, J. Goldstone, S. Gutmann, and M. Sipser, Quantum Computation by Adiabatic Evolution, *arXiv e-prints*, quant-ph/0001106 (2000), arXiv:quant-ph/0001106 [quant-ph].

[14] A. Aspuru-Guzik, A. D. Dutoi, P. J. Love, and M. Head-Gordon, Simulated quantum computation of molecular energies, *Science* **309**, 1704 (2005), <https://www.science.org/doi/pdf/10.1126/science.1113479>.

[15] Y. Nishiyama, H. Nishi, Y. Couzinié, T. Kosugi, and Y.-i. Matsushita, First-quantized adiabatic time evolution for the ground state of a many-electron system and the optimal nuclear configuration, *Phys. Rev. A* **109**, 022423 (2024).

[16] A. Peruzzo, J. McClean, P. Shadbolt, M.-H. Yung, X.-Q. Zhou, P. J. Love, A. Aspuru-Guzik, and J. L. O'Brien, A variational eigenvalue solver on a photonic quantum processor, *Nature communications* **5**, 1 (2014).

[17] E. Farhi, J. Goldstone, and S. Gutmann, A quantum approximate optimization algorithm, *arXiv preprint arXiv:1411.4028* <https://doi.org/10.48550/arXiv.1411.4028> (2014).

[18] Y. Dong, L. Lin, and Y. Tong, Ground-state preparation and energy estimation on early fault-tolerant quantum computers via quantum eigenvalue transformation of unitary matrices, *PRX Quantum* **3**, 040305 (2022).

[19] R. M. Gingrich and C. P. Williams, Non-unitary probabilistic quantum computing, in *Proceedings of the Winter International Symposium on Information and Communication Technologies*, WISICT '04 (Trinity College Dublin, 2004) p. 1–6.

[20] H. Terashima and M. Ueda, Nonunitary quantum circuit, *International Journal of Quantum Information* **3**, 633 (2005).

[21] S. McArdle, T. Jones, S. Endo, Y. Li, S. C. Benjamin, and X. Yuan, Variational ansatz-based quantum simulation of imaginary time evolution, *npj Quantum Information* **5**, 1 (2019).

[22] M. Motta, C. Sun, A. T. Tan, M. J. O'Rourke, E. Ye, A. J. Minnich, F. G. Brandao, and G. K. Chan, Determining eigenstates and thermal states on a quantum computer using quantum imaginary time evolution, *Nature Physics* **16**, 205 (2020).

[23] T. Kosugi, Y. Nishiyama, H. Nishi, and Y.-i. Matsushita, Imaginary-time evolution using forward and backward real-time evolution with a single ancilla: First-quantized eigensolver algorithm for quantum chemistry, *Phys. Rev. Research* **4**, 033121 (2022).

[24] C. Leadbeater, N. Fitzpatrick, D. M. Ramo, and A. J. W. Thom, Non-unitary trotter circuits for imaginary time evolution, *Quantum Science and Technology* **9**, 045007 (2024).

[25] H.-N. Xie, S.-J. Wei, F. Yang, Z.-A. Wang, C.-T. Chen, H. Fan, and G.-L. Long, Probabilistic imaginary-time evolution algorithm based on nonunitary quantum circuits, *Phys. Rev. A* **109**, 052414 (2024).

[26] T. Kosugi and Y.-i. Matsushita, Construction of green's functions on a quantum computer: Quasiparticle spectra of molecules, *Phys. Rev. A* **101**, 012330 (2020).

[27] T. Kosugi and Y.-i. Matsushita, Linear-response functions of molecules on a quantum computer: Charge and spin responses and optical absorption, *Phys. Rev. Research* **2**, 033043 (2020).

[28] S.-N. Sun, B. Marinelli, J. M. Koh, Y. Kim, L. B. Nguyen, L. Chen, J. M. Kreikebaum, D. I. Santiago, I. Siddiqi, and A. J. Minnich, Quantum computation of frequency-domain molecular response properties using a three-qubit itoffoli gate, *npj Quantum Information* **10**, 55 (2024).

[29] R. Sakuma, S. Kanno, K. Sugisaki, T. Abe, and N. Yamamoto, Entanglement-assisted phase estimation algorithm for calculating dynamical response functions, *arXiv e-prints*, arXiv:2404.19554 (2024), arXiv:2404.19554 [quant-ph].

[30] Y. Nakamura, Y. A. Pashkin, and J. Tsai, Coherent control of macroscopic quantum states in a single-cooper-pair box, *nature* **398**, 786 (1999).

[31] F. Arute, K. Arya, R. Babbush, D. Bacon, J. C. Bardin, R. Barends, R. Biswas, S. Boixo, F. G. Brandao, D. A. Buell, *et al.*, Quantum supremacy using a programmable superconducting processor, *Nature* **574**, 505 (2019).

[32] M. Gong, S. Wang, C. Zha, M.-C. Chen, H.-L. Huang, Y. Wu, Q. Zhu, Y. Zhao, S. Li, S. Guo, H. Qian, Y. Ye, F. Chen, C. Ying, J. Yu, D. Fan, D. Wu, H. Su, H. Deng, H. Rong, K. Zhang, S. Cao, J. Lin, Y. Xu, L. Sun, C. Guo, N. Li, F. Liang, V. M. Bastidas, K. Nemoto, W. J. Munro, Y.-H. Huo, C.-Y. Lu, C.-Z. Peng, X. Zhu, and J.-W. Pan, Quantum walks on a programmable two-dimensional 62-qubit superconducting processor, *Science* **372**, 948 (2021), <https://www.science.org/doi/pdf/10.1126/science.abg7812>.

[33] S. A. Moses, C. H. Baldwin, M. S. Allman, R. Acuña, L. Ascarrunz, C. Barnes, J. Bartolotta, B. Bjork, P. Blanchard, M. Bohn, J. G. Bohnet, N. C. Brown, N. Q. Burdick, W. C. Burton, S. L. Campbell, J. P. Campora, C. Carron, J. Chambers, J. W. Chan, Y. H. Chen, A. Chernoguzov, E. Chertkov, J. Colina, J. P. Curtis, R. Daniel, M. DeCross, D. Deen, C. Delaney, J. M. Dreiling, C. T. Ertsgaard, J. Esposito, B. Estey, M. Fabrikant, C. Figgatt, C. Foltz, M. Foss-Feig, D. Francois, J. P. Gaebler, T. M. Gatterman, C. N. Gilbreth, J. Giles, E. Glynn, A. Hall, A. M. Hankin, A. Hansen, D. Hayes, B. Higashi, I. M. Hoffman, B. Horning, J. J. Hout, R. Jacobs, J. Johansen, L. Jones,

J. Karcz, T. Klein, P. Lauria, P. Lee, D. Liefer, S. T. Lu, D. Lucchetti, C. Lytle, A. Malm, M. Matheny, B. Mathewson, K. Mayer, D. B. Miller, M. Mills, B. Neyenhuis, L. Nugent, S. Olson, J. Parks, G. N. Price, Z. Price, M. Pugh, A. Ransford, A. P. Reed, C. Roman, M. Rowe, C. Ryan-Anderson, S. Sanders, J. Sedlacek, P. Shevchuk, P. Siegfried, T. Skripka, B. Spaun, R. T. Sprenkle, R. P. Stutz, M. Swallows, R. I. Tobey, A. Tran, T. Tran, E. Vogt, C. Volin, J. Walker, A. M. Zolot, and J. M. Pino, A race-track trapped-ion quantum processor, *Phys. Rev. X* **13**, 041052 (2023).

[34] M. DeCross, R. Haghshenas, M. Liu, E. Rinaldi, J. Gray, Y. Alexeev, C. H. Baldwin, J. P. Bartolotta, M. Bohn, E. Chertkov, J. Cline, J. Colina, D. DelVento, J. M. Dreiling, C. Foltz, J. P. Gaebler, T. M. Gatterman, C. N. Gilbreth, J. Giles, D. Gresh, A. Hall, A. Hankin, A. Hansen, N. Hewitt, I. Hoffman, C. Holliman, R. B. Hutson, T. Jacobs, J. Johansen, P. J. Lee, E. Lehman, D. Lucchetti, D. Lykov, I. S. Madjarov, B. Mathewson, K. Mayer, M. Mills, P. Niroula, J. M. Pino, C. Roman, M. Schechter, P. E. Siegfried, B. G. Tiemann, C. Volin, J. Walker, R. Shaydulin, M. Pistoia, S. A. Moses, D. Hayes, B. Neyenhuis, R. P. Stutz, and M. Foss-Feig, The computational power of random quantum circuits in arbitrary geometries, *arXiv e-prints*, [arXiv:2406.02501](https://arxiv.org/abs/2406.02501) (2024), [arXiv:2406.02501](https://arxiv.org/abs/2406.02501) [quant-ph].

[35] Y. Chew, T. Tomita, T. P. Mahesh, S. Sugawa, S. de Léséleuc, and K. Ohmori, Ultrafast energy exchange between two single rydberg atoms on a nanosecond timescale, *Nature Photonics* **16**, 724 (2022).

[36] D. Bluvstein, S. J. Evered, A. A. Geim, S. H. Li, H. Zhou, T. Manovitz, S. Ebadi, M. Cain, M. Kalinowski, D. Hangleiter, J. P. Bonilla Ataides, N. Maskara, I. Cong, X. Gao, P. Sales Rodriguez, T. Karolyshyn, G. Semeghini, M. J. Gullans, M. Greiner, V. Vuletić, and M. D. Lukin, Logical quantum processor based on reconfigurable atom arrays, *Nature* **626**, 58 (2024).

[37] H. J. Manetsch, G. Nomura, E. Bataille, K. H. Leung, X. Lv, and M. Endres, A tweezer array with 6100 highly coherent atomic qubits, *arXiv e-prints*, [arXiv:2403.12021](https://arxiv.org/abs/2403.12021) (2024), [arXiv:2403.12021](https://arxiv.org/abs/2403.12021) [quant-ph].

[38] C. N. Self, M. Benedetti, and D. Amaro, Protecting expressive circuits with a quantum error detection code, *Nature Physics* **10**.1038/s41567-023-02282-2 (2024).

[39] R. S. Gupta, N. Sundaresan, T. Alexander, C. J. Wood, S. T. Merkel, M. B. Healy, M. Hillenbrand, T. Jochym-O'Connor, J. R. Wootton, T. J. Yoder, A. W. Cross, M. Takita, and B. J. Brown, Encoding a magic state with beyond break-even fidelity, *Nature* **625**, 259 (2024).

[40] S. Konno, W. Asavanant, F. Hanamura, H. Nagayoshi, K. Fukui, A. Sakaguchi, R. Ide, F. China, M. Yabuno, S. Miki, H. Terai, K. Takase, M. Endo, P. Marek, R. Filip, P. van Loock, and A. Furusawa, Logical states for fault-tolerant quantum computation with propagating light, *Science* **383**, 289 (2024), <https://www.science.org/doi/pdf/10.1126/science.adk7560>.

[41] T. Ichikawa, H. Hakoshima, K. Inui, K. Ito, R. Matsuda, K. Mitarai, K. Miyamoto, W. Mizukami, K. Mizuta, T. Mori, Y. Nakano, A. Nakayama, K. N. Okada, T. Sugimoto, S. Takahira, N. Takemori, S. Tsukano, H. Ueda, R. Watanabe, Y. Yoshida, and K. Fujii, Current numbers of qubits and their uses, *Nature Reviews Physics* **6**, 345 (2024).

[42] Y. Ishiyama, R. Nagai, S. Mieda, Y. Takei, Y. Minato, and Y. Natsume, Noise-robust optimization of quantum machine learning models for polymer properties using a simulator and validated on the ionq quantum computer, *Scientific Reports* **12**, 19003 (2022).

[43] T. Weaving, A. Ralli, W. M. Kirby, P. J. Love, S. Succi, and P. V. Coveney, Benchmarking noisy intermediate scale quantum error mitigation strategies for ground state preparation of the hcl molecule, *Phys. Rev. Res.* **5**, 043054 (2023).

[44] J. Selisko, M. Amsler, C. Wever, Y. Kawashima, G. Samsonidze, R. U. Haq, F. Tacchino, I. Tavernelli, and T. Eckl, Dynamical Mean Field Theory for Real Materials on a Quantum Computer, *arXiv e-prints*, [arXiv:2404.09527](https://arxiv.org/abs/2404.09527) (2024), [arXiv:2404.09527](https://arxiv.org/abs/2404.09527) [cond-mat.str-el].

[45] J. Robledo-Moreno, M. Motta, H. Haas, A. Javadi-Abhari, P. Jurcevic, W. Kirby, S. Martiel, K. Sharma, S. Sharma, T. Shirakawa, I. Sitzdikov, R.-Y. Sun, K. J. Sung, M. Takita, M. C. Tran, S. Yunoki, and A. Mezzacapo, Chemistry Beyond Exact Solutions on a Quantum-Centric Supercomputer, *arXiv e-prints*, [arXiv:2405.05068](https://arxiv.org/abs/2405.05068) (2024), [arXiv:2405.05068](https://arxiv.org/abs/2405.05068) [quant-ph].

[46] K. Seki, Y. Kikuchi, T. Hayata, and S. Yunoki, Simulating Floquet scrambling circuits on trapped-ion quantum computers, *arXiv e-prints*, [arXiv:2405.07613](https://arxiv.org/abs/2405.07613) (2024), [arXiv:2405.07613](https://arxiv.org/abs/2405.07613) [quant-ph].

[47] B. B. Buckley, G. D. Fuchs, L. C. Bassett, and D. D. Awschalom, Spin-light coherence for single-spin measurement and control in diamond, *Science* **330**, 1212 (2010), <https://www.science.org/doi/pdf/10.1126/science.1196436>.

[48] P. Neumann, J. Beck, M. Steiner, F. Rempp, H. Fedder, P. R. Hemmer, J. Wrachtrup, and F. Jelezko, Single-shot readout of a single nuclear spin, *Science* **329**, 542 (2010), <https://www.science.org/doi/pdf/10.1126/science.1189075>.

[49] T. Kimoto and J. A. Cooper, *Fundamentals of Silicon Carbide Technology* (John Wiley & Sons, Ltd, 2014).

[50] H. Matsunami and T. Kimoto, Step-controlled epitaxial growth of sic: High quality homoepitaxy, *Materials Science and Engineering: R: Reports* **20**, 125 (1997), r20.

[51] B. Baliga, Power semiconductor device figure of merit for high-frequency applications, *IEEE Electron Device Letters* **10**, 455 (1989).

[52] T. Kobayashi, T. Okuda, K. Tachiki, K. Ito, Y. ichiro Matsushita, and T. Kimoto, Design and formation of sic (0001)/sio2 interfaces via si deposition followed by low-temperature oxidation and high-temperature nitridation, *Applied Physics Express* **13**, 091003 (2020).

[53] J. R. Weber, W. F. Koehl, J. B. Varley, A. Janotti, B. B. Buckley, C. G. V. de Walle, and D. D. Awschalom, Quantum computing with defects, *Proceedings of the National Academy of Sciences* **107**, 8513 (2010), <https://www.pnas.org/doi/pdf/10.1073/pnas.1003052107>.

[54] J. R. Weber, W. F. Koehl, J. B. Varley, A. Janotti, B. B. Buckley, C. G. Van de Walle, and D. D. Awschalom, Defects in SiC for quantum computing, *Journal of Applied Physics* **109**, 102417 (2011), https://pubs.aip.org/aip/jap/article-pdf/doi/10.1063/1.3578264/15074320/102417_1_online.pdf.

[55] W. F. Koehl, B. B. Buckley, F. J. Heremans, G. Calusine, and D. D. Awschalom, Room temperature coherent control of defect spin qubits in silicon carbide, *Nature* **479**, 84 (2011).

[56] A. L. Falk, B. B. Buckley, G. Calusine, W. F. Koehl, V. V. Dobrovitski, A. Politi, C. A. Zorman, P. X.-L. Feng, and D. D. Awschalom, Polytype control of spin qubits in silicon carbide, *Nature Communications* **4**, 1819 (2013).

[57] L. Gordon, J. R. Weber, J. B. Varley, A. Janotti, D. D. Awschalom, and C. G. Van de Walle, Quantum computing with defects, *MRS Bulletin* **38**, 802 (2013).

[58] M. Widmann, S.-Y. Lee, T. Rendler, N. T. Son, H. Fedder, S. Paik, L.-P. Yang, N. Zhao, S. Yang, I. Booker, A. Denisenko, M. Jamali, S. A. Momenzadeh, I. Gerhardt, T. Ohshima, A. Gali, E. Janzén, and J. Wrachtrup, Coherent control of single spins in silicon carbide at room temperature, *Nature Materials* **14**, 164 (2015).

[59] J. Carlos Rojo, G. A. Slack, K. Morgan, B. Raghothamachar, M. Dudley, and L. J. Schowalter, Report on the growth of bulk aluminum nitride and subsequent substrate preparation, *Journal of Crystal Growth* **231**, 317 (2001), proceedings of the International Specialist Meeting on Bulk Nitrides and Related Techniques.

[60] M. Bickermann, B. M. Epelbaum, O. Filip, P. Heimann, S. Nagata, and A. Winnacker, Uv transparent single-crystalline bulk aln substrates, *physica status solidi c* **7**, 21 (2010), <https://onlinelibrary.wiley.com/doi/pdf/10.1002/pssc.200982601>.

[61] H. Okumura, T. Kimoto, and J. Suda, Reduction of threading dislocation density in 2h-aln grown on 6h-sic(0001) by minimizing unintentional active-nitrogen exposure before growth, *Applied Physics Express* **4**, 025502 (2011).

[62] Y. Taniyasu, M. Kasu, and T. Makimoto, Electrical conduction properties of n-type si-doped aln with high electron mobility (i 100cm 2 v $^{-1}$ 1s $^{-1}$), *Applied Physics Letters* **85**, 4672 (2004), https://pubs.aip.org/aip/apl/article-pdf/85/20/4672/18600132/4672_1_online.pdf.

[63] J. Li, K. B. Nam, M. L. Nakarmi, J. Y. Lin, H. X. Jiang, P. Carrier, and S.-H. Wei, Band structure and fundamental optical transitions in wurtzite AlN, *Applied Physics Letters* **83**, 5163 (2003), https://pubs.aip.org/aip/apl/article-pdf/83/25/5163/18584723/5163_1_online.pdf.

[64] J. B. Varley, A. Janotti, and C. G. Van de Walle, Defects in aln as candidates for solid-state qubits, *Phys. Rev. B* **93**, 161201 (2016).

[65] H. Seo, H. Ma, M. Govoni, and G. Galli, Designing defect-based qubit candidates in wide-gap binary semiconductors for solid-state quantum technologies, *Phys. Rev. Mater.* **1**, 075002 (2017).

[66] H. Nishi, T. Kosugi, Y. Nishiya, and Y.-i. Matsushita, Quadratic acceleration of multistep probabilistic algorithms for state preparation, *Phys. Rev. Res.* **6**, L022041 (2024).

[67] J. M. Pino, J. M. Dreiling, C. Figgatt, J. P. Gaebler, S. A. Moses, M. S. Allman, C. H. Baldwin, M. Foss-Feig, D. Hayes, K. Mayer, C. Ryan-Anderson, and B. Neyenhuis, Demonstration of the trapped-ion quantum ccd computer architecture, *Nature* **592**, 209 (2021).

[68] C. Ryan-Anderson, N. C. Brown, M. S. Allman, B. Arkin, G. Asa-Attuah, C. Baldwin, J. Berg, J. G. Bohnet, S. Braxton, N. Burdick, J. P. Campora, A. Chernoguzov, J. Esposito, B. Evans, D. Francois, J. P. Gaebler, T. M. Gatterman, J. Gerber, K. Gilmore, D. Gresh, A. Hall, A. Hankin, J. Hostetter, D. Lucchetti, K. Mayer, J. Myers, B. Neyenhuis, J. Santago, J. Sedlacek, T. Skripka, A. Slattery, R. P. Stutz, J. Tait, R. Tobey, G. Vittorini, J. Walker, and D. Hayes, Implementing Fault-tolerant Entangling Gates on the Five-qubit Code and the Color Code, *arXiv e-prints*, [arXiv:2208.01863](https://arxiv.org/abs/2208.01863) (2022), [arXiv:2208.01863](https://arxiv.org/abs/2208.01863) [quant-ph].

[69] F. Aryasetiawan, M. Imada, A. Georges, G. Kotliar, S. Biermann, and A. I. Lichtenstein, Frequency-dependent local interactions and low-energy effective models from electronic structure calculations, *Phys. Rev. B* **70**, 195104 (2004).

[70] M. Imada and T. Miyake, Electronic structure calculation by first principles for strongly correlated electron systems, *Journal of the Physical Society of Japan* **79**, 112001 (2010), <https://doi.org/10.1143/JPSJ.79.112001>.

[71] P. Hohenberg and W. Kohn, Inhomogeneous electron gas, *Phys. Rev.* **136**, B864 (1964).

[72] W. Kohn and L. J. Sham, Self-consistent equations including exchange and correlation effects, *Phys. Rev.* **140**, A1133 (1965).

[73] A. M. Steane, Simple quantum error-correcting codes, *Phys. Rev. A* **54**, 4741 (1996).

[74] D. Gottesman, Theory of fault-tolerant quantum computation, *Phys. Rev. A* **57**, 127 (1998).

[75] E. Knill, Fault-Tolerant Postselected Quantum Computation: Schemes, *arXiv e-prints*, [quant-ph/0402171](https://arxiv.org/abs/quant-ph/0402171) (2004), [arXiv:quant-ph/0402171](https://arxiv.org/abs/quant-ph/0402171) [quant-ph].

[76] E. Knill, Fault-Tolerant Postselected Quantum Computation: Threshold Analysis, *arXiv e-prints*, [quant-ph/0404104](https://arxiv.org/abs/quant-ph/0404104) (2004), [arXiv:quant-ph/0404104](https://arxiv.org/abs/quant-ph/0404104) [quant-ph].

[77] N. Troullier and J. L. Martins, Efficient pseudopotentials for plane-wave calculations, *Phys. Rev. B* **43**, 1993 (1991).

[78] D. R. Hamann, Optimized norm-conserving vanderbilt pseudopotentials, *Phys. Rev. B* **88**, 085117 (2013).

[79] M. Schlipf and F. Gygi, Optimization algorithm for the generation of oncv pseudopotentials, *Computer Physics Communications* **196**, 36 (2015).

[80] P. Giannozzi, S. Baroni, N. Bonini, M. Calandra, R. Car, C. Cavazzoni, D. Ceresoli, G. L. Chiarotti, M. Cococcioni, I. Dabo, A. D. Corso, S. de Gironcoli, S. Fabris, G. Fratesi, R. Gebauer, U. Gerstmann, C. Gougaudis, A. Kokalj, M. Lazzeri, L. Martin-Samos, N. Marzari, F. Mauri, R. Mazzarello, S. Paolini, A. Pasquarello, L. Paulatto, C. Sbraccia, S. Scandolo, G. Sclauzero, A. P. Seitsonen, A. Smogunov, P. Umari, and R. M. Wentzcovitch, Quantum espresso: a modular and open-source software project for quantum simulations of materials, *Journal of Physics: Condensed Matter* **21**, 395502 (2009).

[81] P. Giannozzi, O. Andreussi, T. Brumme, O. Bunau, M. B. Nardelli, M. Calandra, R. Car, C. Cavazzoni, D. Ceresoli, M. Cococcioni, N. Colonna, I. Carnimeo, A. D. Corso, S. de Gironcoli, P. Delugas, R. A. DiStasio, A. Ferretti, A. Floris, G. Fratesi, G. Fugallo, R. Gebauer, U. Gerstmann, F. Giustino,

T. Gorni, J. Jia, M. Kawamura, H.-Y. Ko, A. Kokalj, E. Küçükbenli, M. Lazzeri, M. Marsili, N. Marzari, F. Mauri, N. L. Nguyen, H.-V. Nguyen, A. O. de-la Roza, L. Paulatto, S. Poncé, D. Rocca, R. Sabatini, B. Santra, M. Schlipf, A. P. Seitsonen, A. Smogunov, I. Timrov, T. Thonhauser, P. Umari, N. Vast, X. Wu, and S. Baroni, Advanced capabilities for materials modelling with quantum espresso, *Journal of Physics: Condensed Matter* **29**, 465901 (2017).

[82] P. Giannozzi, O. Baseggio, P. Bonfà, D. Brunato, R. Car, I. Carnimeo, C. Cavazzoni, S. de Gironcoli, P. Delugas, F. Ferrari Ruffino, A. Ferretti, N. Marzari, I. Timrov, A. Urru, and S. Baroni, Quantum ESPRESSO toward the exascale, *The Journal of Chemical Physics* **152**, 154105 (2020), https://pubs.aip.org/aip/jcp/article-pdf/doi/10.1063/5.0005082/16721881/154105_1_online.pdf.

[83] J. P. Perdew, K. Burke, and M. Ernzerhof, Generalized gradient approximation made simple, *Phys. Rev. Lett.* **77**, 3865 (1996).

[84] J. Heyd, G. E. Scuseria, and M. Ernzerhof, Hybrid functionals based on a screened Coulomb potential, *The Journal of Chemical Physics* **118**, 8207 (2003), https://pubs.aip.org/aip/jcp/article-pdf/118/18/8207/19093575/8207_1_online.pdf.

[85] J. Heyd, G. E. Scuseria, and M. Ernzerhof, Erratum: “Hybrid functionals based on a screened Coulomb potential” [J. Chem. Phys. 118, 8207 (2003)], *The Journal of Chemical Physics* **124**, 219906 (2006), https://pubs.aip.org/aip/jcp/article-pdf/doi/10.1063/1.2204597/15387022/219906_1_online.pdf.

[86] K. Ido, M. Kawamura, Y. Motoyama, K. Yoshimi, Y. Yamaji, S. Todo, N. Kawashima, and T. Misawa, Update of HF: Newly added functions and methods in versions 2 and 3, *Computer Physics Communications* **298**, 109093 (2024).

[87] K. Nakamura, Y. Yoshimoto, Y. Nomura, T. Tadano, M. Kawamura, T. Kosugi, K. Yoshimi, T. Misawa, and Y. Motoyama, Respack: An ab initio tool for derivation of effective low-energy model of material, *Computer Physics Communications* **261**, 107781 (2021).

[88] P. Jordan and E. Wigner, Über das paulische äquivalenzverbot, *Zeitschrift für Physik* **47**, 631 (1928).

[89] S. B. Bravyi and A. Y. Kitaev, Fermionic quantum computation, *Annals of Physics* **298**, 210 (2002).

[90] J. T. Seeley, M. J. Richard, and P. J. Love, The Bravyi-Kitaev transformation for quantum computation of electronic structure, *The Journal of Chemical Physics* **137**, 224109 (2012), https://pubs.aip.org/aip/jcp/article-pdf/doi/10.1063/1.4768229/13999577/224109_1_online.pdf.

[91] S. Bravyi, J. M. Gambetta, A. Mezzacapo, and K. Temme, Tapering off qubits to simulate fermionic Hamiltonians, *arXiv e-prints*, arXiv:1701.08213 (2017), [arXiv:1701.08213 \[quant-ph\]](https://arxiv.org/abs/1701.08213).

[92] P. J. J. O’Malley, R. Babbush, I. D. Kivlichan, J. Romero, J. R. McClean, R. Barends, J. Kelly, P. Roushan, A. Tranter, N. Ding, B. Campbell, Y. Chen, Z. Chen, B. Chiaro, A. Dunsworth, A. G. Fowler, E. Jeffrey, E. Lucero, A. Megrant, J. Y. Mutus, M. Neeley, C. Neill, C. Quintana, D. Sank, A. Vainsencher, J. Wenner, T. C. White, P. V. Coveney, P. J. Love, H. Neven, A. Aspuru-Guzik, and J. M. Martinis, Scalable quantum simulation of molecular energies, *Phys. Rev. X* **6**, 031007 (2016).

[93] S. Paesani, A. A. Gentile, R. Santagati, J. Wang, N. Wiebe, D. P. Tew, J. L. O’Brien, and M. G. Thompson, Experimental bayesian quantum phase estimation on a silicon photonic chip, *Phys. Rev. Lett.* **118**, 100503 (2017).

[94] L. Lin and Y. Tong, Heisenberg-limited ground-state energy estimation for early fault-tolerant quantum computers, *PRX Quantum* **3**, 010318 (2022).

[95] K. Yamamoto, S. Duffield, Y. Kikuchi, and D. Muñoz Ramo, Demonstrating bayesian quantum phase estimation with quantum error detection, *Phys. Rev. Res.* **6**, 013221 (2024).

[96] K. Mølmer and A. Sørensen, Multiparticle entanglement of hot trapped ions, *Phys. Rev. Lett.* **82**, 1835 (1999).

[97] A. Khindanov, Y. Yao, and T. Iadecola, Robust preparation of ground state phases under noisy imaginary time evolution, *arXiv e-prints*, arXiv:2406.04285 (2024), [arXiv:2406.04285 \[quant-ph\]](https://arxiv.org/abs/2406.04285).

[98] R. Chao and B. W. Reichardt, Quantum error correction with only two extra qubits, *Phys. Rev. Lett.* **121**, 050502 (2018).

[99] M. Suzuki, General theory of fractal path integrals with applications to many-body theories and statistical physics, *Journal of Mathematical Physics* **32**, 400 (1991).

[100] M. Bockstedte, F. Schütz, T. Garratt, V. Ivády, and A. Gali, Ab initio description of highly correlated states in defects for realizing quantum bits, *npj Quantum Materials* **3**, 31 (2018).

[101] G. Knizia and G. K.-L. Chan, Density matrix embedding: A simple alternative to dynamical mean-field theory, *Phys. Rev. Lett.* **109**, 186404 (2012).

[102] S. Wouters, C. A. Jiménez-Hoyos, Q. Sun, and G. K.-L. Chan, A practical guide to density matrix embedding theory in quantum chemistry, *Journal of Chemical Theory and Computation* **12**, 2706 (2016), pMID: 27159268, <https://doi.org/10.1021/acs.jctc.6b00316>.

[103] H. Q. Pham, M. R. Hermes, and L. Gagliardi, Periodic electronic structure calculations with the density matrix embedding theory, *Journal of Chemical Theory and Computation* **16**, 130 (2020), pMID: 31815455, <https://doi.org/10.1021/acs.jctc.9b00939>.

[104] H. Ma, M. Govoni, and G. Galli, Quantum simulations of materials on near-term quantum computers, *npj Computational Materials* **6**, 85 (2020).

[105] H. Ma, N. Sheng, M. Govoni, and G. Galli, Quantum embedding theory for strongly correlated states in materials, *Journal of Chemical Theory and Computation* **17**, 2116 (2021).

[106] B. Huang, M. Govoni, and G. Galli, Simulating the electronic structure of spin defects on quantum computers, *PRX Quantum* **3**, 010339 (2022).

[107] G. Davies, M. F. Hamer, and W. C. Price, Optical studies of the 1.945 ev vibronic band in diamond, *Proceedings of the Royal Society of London. A. Mathematical and Physical Sciences* **348**, 285 (1976), <https://royalsocietypublishing.org/doi/pdf/10.1098/rspa.1976.0039>.

[108] L. J. Rogers, S. Armstrong, M. J. Sellars, and N. B. Manson, Infrared emission of the nv centre in diamond: Zeeman and uniaxial stress studies, *New Journal of Physics* **10**, 103024 (2008).

[109] G. m. H. Thiering and A. Gali, Ab initio calculation of spin-orbit coupling for an nv center in diamond exhibit-

ing dynamic jahn-teller effect, *Phys. Rev. B* **96**, 081115 (2017).

[110] C. Freysoldt, J. Neugebauer, and C. G. Van de Walle, Fully ab initio finite-size corrections for charged-defect supercell calculations, *Phys. Rev. Lett.* **102**, 016402 (2009).

[111] Qiskit contributors, *Qiskit: An open-source framework for quantum computing* (2023).

[112] S. Sivarajah, S. Dilkes, A. Cowtan, W. Simmons, A. Edgington, and R. Duncan, $t\text{-ket}\rangle$: a retargetable compiler for nisq devices, *Quantum Science and Technology* **6**, 014003 (2020).

[113] System model h1 powered by honeywell, Available at <https://www.quantinuum.com/hardware/h1> (2024).

[114] H. Nishi, K. Hamada, Y. Nishiya, T. Kosugi, and Y.-i. Matsushita, Optimal scheduling in probabilistic imaginary-time evolution on a quantum computer, *Phys. Rev. Res.* **5**, 043048 (2023).

[115] Y. Ge, J. Tura, and J. I. Cirac, Faster ground state preparation and high-precision ground energy estimation with fewer qubits, *Journal of Mathematical Physics* **60**, 022202 (2019).

[116] K. Choi, D. Lee, J. Bonitati, Z. Qian, and J. Watkins, Rodeo algorithm for quantum computing, *Phys. Rev. Lett.* **127**, 040505 (2021).

[117] M. A. Nielsen, I. L. Chuang, I. L. Chuang, *et al.*, *Quantum Computation and Quantum Information* (Cambridge University Press, 2000).

[118] R. Meister and S. C. Benjamin, Resource-frugal hamiltonian eigenstate preparation via repeated quantum phase estimation measurements (2022).

[119] T. Kosugi, H. Nishi, and Y. ichiro Matsushita, First-quantized eigensolver for ground and excited states of electrons under a uniform magnetic field, *Japanese Journal of Applied Physics* **62**, 062004 (2023).

[120] N. Yoshioka, T. Okubo, Y. Suzuki, Y. Koizumi, and W. Mizukami, Hunting for quantum-classical crossover in condensed matter problems, *npj Quantum Information* **10**, 45 (2024).

[121] O. Madelung, *Semiconductors—basic data* (Springer Science & Business Media, 2012).

[122] H. Seo, M. Govoni, and G. Galli, Design of defect spins in piezoelectric aluminum nitride for solid-state hybrid quantum technologies, *Scientific Reports* **6**, 20803 (2016).

[123] P. Rinke, M. Winkelnkemper, A. Qteish, D. Bimberg, J. Neugebauer, and M. Scheffler, Consistent set of band parameters for the group-iii nitrides aln, gan, and inn, *Phys. Rev. B* **77**, 075202 (2008).

[124] Y. Yoshida, N. Takemori, and W. Mizukami, Ab initio extended Hubbard model of short polyenes for efficient quantum computing, *arXiv e-prints*, arXiv:2404.01623 (2024), arXiv:2404.01623 [quant-ph].

[125] V. Ivády, I. A. Abrikosov, and A. Gali, First principles calculation of spin-related quantities for point defect qubit research, *npj Computational Materials* **4**, 76 (2018).

[126] Y. Ma, M. Rohlfing, and A. Gali, Excited states of the negatively charged nitrogen-vacancy color center in diamond, *Phys. Rev. B* **81**, 041204 (2010).

[127] P. Delaney, J. C. Greer, and J. A. Larsson, Spin-polarization mechanisms of the nitrogen-vacancy center in diamond, *Nano Letters* **10**, 610 (2010).

[128] A. Ranjbar, M. Babamoradi, M. Heidari Saani, M. A. Vesaghi, K. Esfarjani, and Y. Kawazoe, Many-electron states of nitrogen-vacancy centers in diamond and spin density calculations, *Phys. Rev. B* **84**, 165212 (2011).

[129] S. Choi, M. Jain, and S. G. Louie, Mechanism for optical initialization of spin in nv^- center in diamond, *Phys. Rev. B* **86**, 041202 (2012).

[130] N. Sheng, C. Vorwerk, M. Govoni, and G. Galli, Green's function formulation of quantum defect embedding theory, *Journal of Chemical Theory and Computation* **18**, 3512 (2022), PMID: 35648660, <https://doi.org/10.1021/acs.jctc.2c00240>.

[131] Y. Jin, V. W.-z. Yu, M. Govoni, A. C. Xu, and G. Galli, Excited state properties of point defects in semiconductors and insulators investigated with time-dependent density functional theory, *Journal of Chemical Theory and Computation* **19**, 8689 (2023).

Appendix A: Computational details of the DFT calculation

1. Lattice parameters

The lattice constant of diamond was calculated as $a = 3.534 \text{ \AA}$, which was obtained from spin-restricted DFT calculations with PBE functional. The calculated lattice constant is in good agreement with the experimental value of $a = 3.567 \text{ \AA}$ [121]. The calculated band gap is $E_g = 4.19 \text{ eV}$, which underestimates the experimental value of $E_g = 5.45\text{--}5.50 \text{ eV}$. This underestimation can be improved to $E_g = 5.39 \text{ eV}$ by using the screened hybrid functional of Heyd, Scuseria, and Ernzerhof (HSE) [84, 85], starting from a structure with a lattice constant of $a = 3.534 \text{ \AA}$.

We used the previously reported structural properties of w-AlN: $a = 3.130 \text{ \AA}$, $c/a = 1.603$, and $u = 0.382$ [122]. The experimental values were $a = 3.110 \text{ \AA}$, $c/a = 1.601$, and $u = 0.382$ [123]. However, similar to diamond, the band gap is underestimated by our calculation with the PBE function, as $E_g = 4.09 \text{ eV}$. This underestimation was also improved by the HSE function, as in $E_g = 5.36 \text{ eV}$. The lattice parameters computed in the DFT calculation with the PBE function are used in the supercell calculation in the main text.

2. Convergence of the system size of w-AlN

The convergence of supercell size was examined by varying the number of unit cells in the supercell. Supercells containing 96, 240, or 360 atoms were used. The k -point sampling convergence was studied using Monkhorst-Pack grids. The densities of k -points were taken as $1 \times 1 \times 1$ and $2 \times 2 \times 2$. The total energy, band gap, and single-particle states in the band gap are shown in Fig. 9.

Similar to a previous investigation of the numerical error in the negatively nitrogen vacancy (V_N^{-1}) in w-AlN [122], we also observed that Γ -point sampling is not sufficient in a 96-atoms supercell. However, a slight difference in the quantities between Γ and $2 \times 2 \times 2$ k -point sampling was observed in the 240-atoms supercell. In Fig. 9(b), the band gap decreases and converges to 4.10 eV, which is close to the value of perfect crystal of w-AlN, $E_g = 4.09$ eV. Although single-particle states e_x and e_y have a small splitting in the 96-atoms supercell calculation in Fig. 9 (e) and (f), these two states close each other and almost degenerate at 240-atom supercell. Accordingly, we choose a 240-atoms supercell and Γ point sampling in the main text.

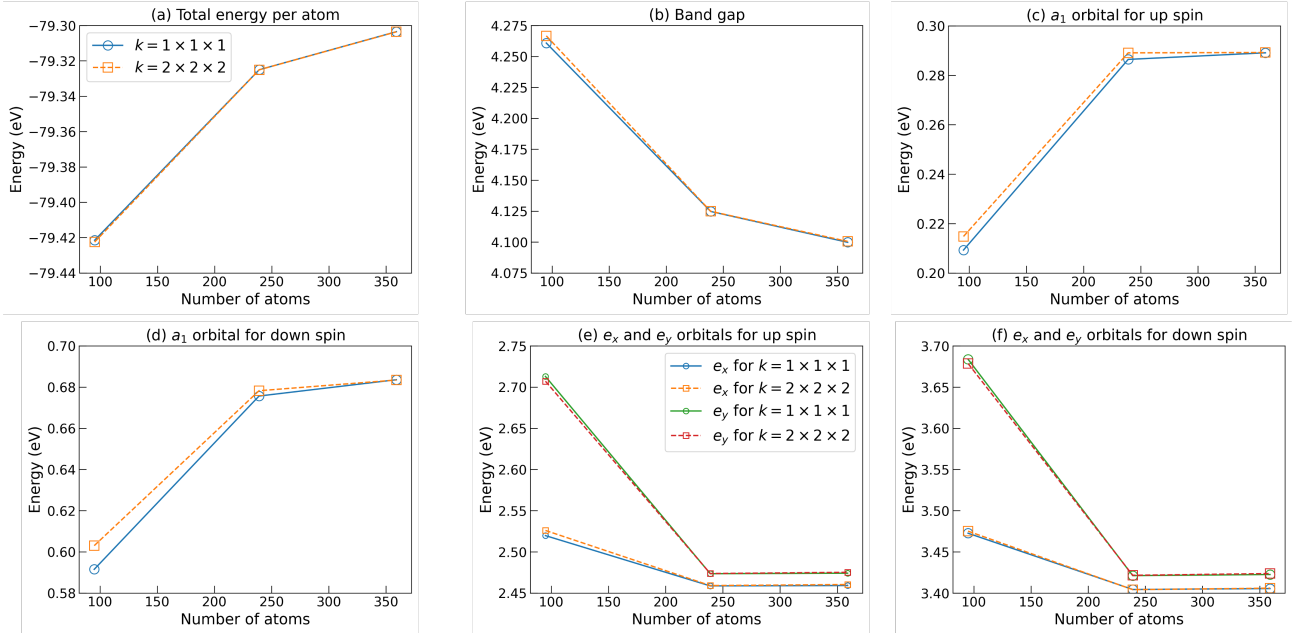


FIG. 9. Numerical errors of the defect calculation for $(Zr_{Al}VN)^0$ complex in w-AlN introduced by the supercell size and k -point sampling. (a) Total energy per atom, (b) band gap, and (c)–(f) single-particle states calculated using the spin-unrestricted KS equation as a function of supercell size and k -point sampling. 96-, 240-, and 360-atoms supercell were used. All points were calculated with the PBE functional and plane-wave cutoff of 75 Ry.

3. Convergence of constructing the low-energy effective Hamiltonian

We investigated the convergence of the vertical excitation energy for the NV^- -center in diamond as a function of the parameters contained in the RESPACK software [87] when an effective low-energy model was constructed. The KS wave function as an input for the RESPACK calculation was obtained by spin-restricted DFT calculation with the PBE functional starting from the optimized structure of the 216-atom supercell. Note that we increased the energy cutoff of the plane-wave basis sets from 50 to 100 Ry to properly describe the high-energy states. An insufficient energy cutoff induces symmetry breaking of the effective Hamiltonian, for example, for all (i, j) pairs, where $i \neq j$ and Coulomb integrals V_{ij} are the same, whereas screened Coulomb integrals U_{ij} are different from each other. For example, in this case, the degeneracy of 1E state is broken.

We varied two parameters: the number of bands, N_{band} and the cutoff energy for the dielectric function, $E_{\text{cut}}^{\varepsilon}$. The FCI energy is fitted by [124]

$$f(x) = b \times \exp(-x/c) + \Delta E_{\infty} \quad (\text{A1})$$

where b and c are real numbers and ΔE_{∞} denotes the extrapolated excitation energy. We consider x as the number of bands N_{band} in Fig. 10(a) and the cutoff energy for dielectric function $E_{\text{cut}}^{\varepsilon}$ in Fig. 10(b).

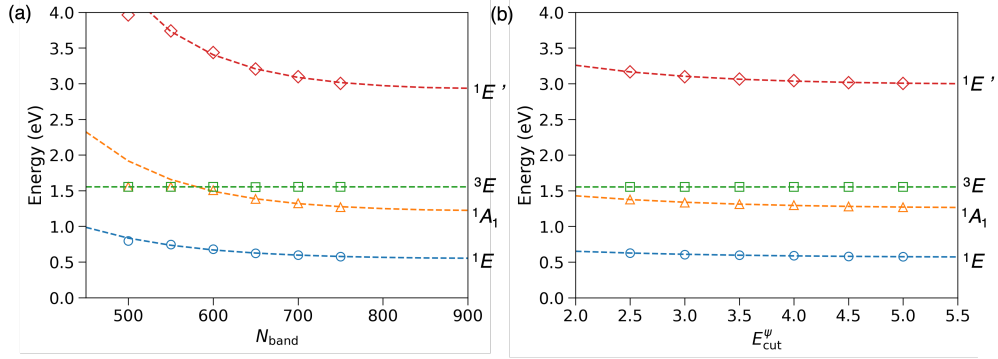


FIG. 10. FCI energies for the NV^- -center in diamond as a function of (a) number of bands, N_{band} , and (b) cutoff energy for the dielectric function, E_{cut}^e . A 216-atom supercell and Γ point sampling were used. All points were calculated with a PBE functional and plane-wave cutoff of 100 Ry.

The dependence of the FCI energy on N_{band} is plotted in Fig. 10(a), where E_{cut}^e is fixed to 5.0 eV. In a small number of bands, such as $N_{\text{band}} = 500 - 550$, 3E and 1A_1 states are almost degenerate because of the lack of inclusion of high-energy bands. Increasing N_{band} decreases the excitation energy, and we almost reach convergence at $N_{\text{band}} = 750$. We fitted equation (A1) at three points: 650, 700, and 750. The results obtained at $N_{\text{band}} = 750$ (0.57/1.27/1.55 eV for $^1E/^1A_1/^3E$ states) are different from the extrapolated results ΔE_∞ (0.54/1.20/1.55 eV for $^1E/^1A_1/^3E$ states) within 0.07 eV.

Figure 10(b) shows the dependence of excitation energy on E_{cut}^e , where $N_{\text{band}} = 750$. Unlike Fig. 10(a), the excitation energy does not vary much with respect to E_{cut}^e . The results obtained at $E_{\text{cut}}^e = 3.0$ Ry (0.61/1.33/1.55 eV for $^1E/^1A_1/^3E$ states) is sufficiently converged to the extrapolated results (0.56/1.25/1.55 eV for $^1E/^1A_1/^3E$ states). It is known that E_{cut}^e should be 0.1 times the kinetic energy cut-off used in the DFT calculation [87] however, the results in Fig. 10(b) show that a reduction to 0.06 times is valid.

Appendix B: Comparison of vertical excitation energy with other methods

The previous numerical results for the exciton energy for NV center diamonds are summarized in Table IV. See also the review paper on spin-defect calculations [125].

TABLE IV. Computed vertical excitation energies (eV) of the negatively charged NV^- -center in diamond.

Method	$^3A_2 \rightarrow ^3E$	$^1E \rightarrow ^1A_1$	$^1A_1 \rightarrow ^3E$	$^3A_2 \rightarrow ^1A_1$	$^3A_2 \rightarrow ^1E$
GW+BSE [126]	2.09	0.59	1.10	0.4	0.99
CI on $\text{C}_{42}\text{H}_{42}\text{N}$ [127]	1.93	1.43	-0.1	1.94	0.51
Ext. Hubb. + DFT par. [128]	2.38	0.62	1.35	0.41	1.03
Ext. Hubb. + GW fit. [129]	2.0	0.96	0.6	1.4	0.44
CI + cRPA [100]	2.05	0.89	0.69	1.36	0.47
CI + RPA [104]	1.92	0.9	0.55	1.37	0.47
CI + beyond-RPA [104]	2.00	1.2	0.24	1.76	0.56
QDET [130]	2.15	0.81	0.88	1.27	0.46
TDDFT (DDH) [131]	2.11	1.4	0.15	1.96	0.56
This study (PBE + Ext. Hubb + CI)	1.55	0.73	0.22	1.33	0.6
This study (HSE + Ext. Hubb + CI)	2.12	0.82	0.66	1.46	0.64
Experiment	1.945 [107]	1.190 [108]	≈ 0.4 [109]		

Appendix C: Model parameters

1. Model parameters of the low-energy effective Hamiltonian

We summarized the model parameters of the low-energy effective Hamiltonian for $(\text{Zr}_{\text{Al}}\text{V}_\text{N})^0$, $(\text{Hf}_{\text{Al}}\text{V}_\text{N})^0$, $(\text{Ti}_{\text{Al}}\text{V}_\text{N})^0$ complexes in w-AlN, and the NV⁻-center in diamond in Table C. The model parameters were obtained using **RESPACK** [87]. The KS wave functions as an input of **RESPACK** were obtained by spin-restricted DFT calculations with the PBE and HSE functional starting from the optimized structure. We used cutoff energies for the dielectric functions of 3.0 Ry and 4.5 Ry for the NV center in diamond and complex defects in w-AlN, respectively. The energy bands are considered for 750 and 1300 bands for the NV⁻-center in diamond and complex defects in w-AlN, respectively.

TABLE V. Model parameters of the low-energy effective Hamiltonian for $(\text{Zr}_{\text{Al}}\text{V}_\text{N})^0$, $(\text{Hf}_{\text{Al}}\text{V}_\text{N})^0$, $(\text{Ti}_{\text{Al}}\text{V}_\text{N})^0$ complexes in w-AlN, and NV⁻-center in diamond. The unit of t_{ij} , U_{ij} , and J_{ij} is eV. The parameters have symmetry as $(i, j) = (j, i)$.

System	(i, j)	t_{ij} (HSE)	U_{ij} (HSE)	J_{ij} (HSE)	t_{ij} (PBE)	U_{ij} (PBE)	J_{ij} (PBE)
ZrV in w-AlN	(1,1)	11.0490	2.6258		11.3439	2.0787	
	(2,2)	11.1031	2.5854		11.3867	2.0493	
	(3,3)	11.0487	2.6258		11.3459	2.0787	
	(1,2)	-0.9938	1.8957	0.2009	-0.7930	1.4343	0.1754
	(1,3)	1.0312	1.9006	0.1945	0.8253	1.4382	0.1695
	(2,3)	0.9940	1.8957	0.2009	0.7920	1.4344	0.1754
HfV in w-AlN	(1,1)	11.1122	2.5571		11.4455	2.0622	
	(2,2)	11.1748	2.5520		11.4966	2.0282	
	(3,3)	11.1134	2.5571		11.4469	2.0622	
	(1,2)	-1.0240	1.9095	0.1912	-0.8384	1.4148	0.1796
	(1,3)	1.0660	1.9088	0.1893	0.8769	1.4299	0.1742
	(2,3)	1.0234	1.9096	0.1912	0.8378	1.4149	0.1797
TiV in w-AlN	(1,1)	10.8699	2.6249		11.2003	2.0793	
	(2,2)	10.9352	2.6285		11.2463	2.0843	
	(3,3)	10.8700	2.6249		11.2005	2.0793	
	(1,2)	-0.9840	2.0563	0.2244	-0.7986	1.5643	0.1998
	(1,3)	1.0236	2.0563	0.2241	0.8308	1.5651	0.1994
	(2,3)	0.9840	2.0563	0.2244	0.7985	1.5643	0.1998
NV in diamond	(1,1), (2,2), (3,3)	15.3843	3.1241		15.6472	2.6656	
	(1,2)	-0.7049	1.0826	0.1416	-0.5176	0.8431	0.1635
	(1,3), (2,3)	0.7049	1.0826	0.1416	0.5176	0.8431	0.1635

2. Specific expression of Hamiltonian

The generator of the CRTE used in the main text is divided into a diagonal part Λ and a non-diagonal part V : $\mathcal{H} \otimes Z = \Lambda + V$. The diagonal part Λ is divided as $\Lambda = \Lambda_1 + \Lambda_2$, where

$$\Lambda_1 = h_{IIZZ}Z_1Z_0 + h_{IZIZ}Z_2Z_0 + h_{ZIZZ}Z_3Z_1Z_0 \quad (\text{C1})$$

and

$$\Lambda_2 = h_{ZZIZ}Z_3Z_2Z_0 + h_{ZIIZ}Z_3Z_0 + h_{IZZZ}Z_2Z_1Z_0 + h_{ZZZZ}Z_3Z_2Z_1Z_0. \quad (\text{C2})$$

The non-diagonal part V is divided as $V = V_1 + V_2$, where

$$\begin{aligned} V_1 = & h_{XXXZ}X_3X_2X_1Z_0 + h_{ZZXZ}Z_3Z_2X_1Z_0 + h_{ZXZZ}Z_3X_2Z_1Z_0 + h_{XZZZ}X_3Z_2Z_1Z_0 + h_{IXXZ}X_2X_1Z_0 \\ & + h_{ZXXZ}Z_3X_2X_1Z_0 + h_{XZXZ}X_3Z_2X_1Z_0 + h_{XIXZ}X_3X_1Z_0 + h_{XXZZ}X_3X_2Z_1Z_0 + h_{XXIZ}X_3X_2Z_0 \\ & + h_{IIXZ}X_1Z_0 + h_{IXIZ}X_2Z_0 + h_{XIIZ}X_3Z_0 + h_{IXZZ}X_2Z_1Z_0 + h_{ZXIZ}Z_3X_2Z_0 \end{aligned} \quad (\text{C3})$$

and

$$\begin{aligned} V_2 = & h_{YYXZ}Y_3Y_2X_1Z_0 + h_{YXYZ}Y_3X_2Y_1Z_0 + h_{XYYZ}X_3Y_2Y_1Z_0 + h_{IZXZ}Z_2X_1Z_0 + h_{YZYZ}Y_3Z_2Y_1Z_0 \\ & + h_{YIYZ}Y_3Y_1Z_0 + h_{YYZZ}Y_3Y_2Z_1Z_0 + h_{YYIZ}Y_3Y_2Z_0 + h_{ZIXZ}Z_3X_1Z_0 + h_{XIZZ}X_3Z_1Z_0 + h_{XZIZ}X_3Z_2Z_0. \end{aligned} \quad (\text{C4})$$

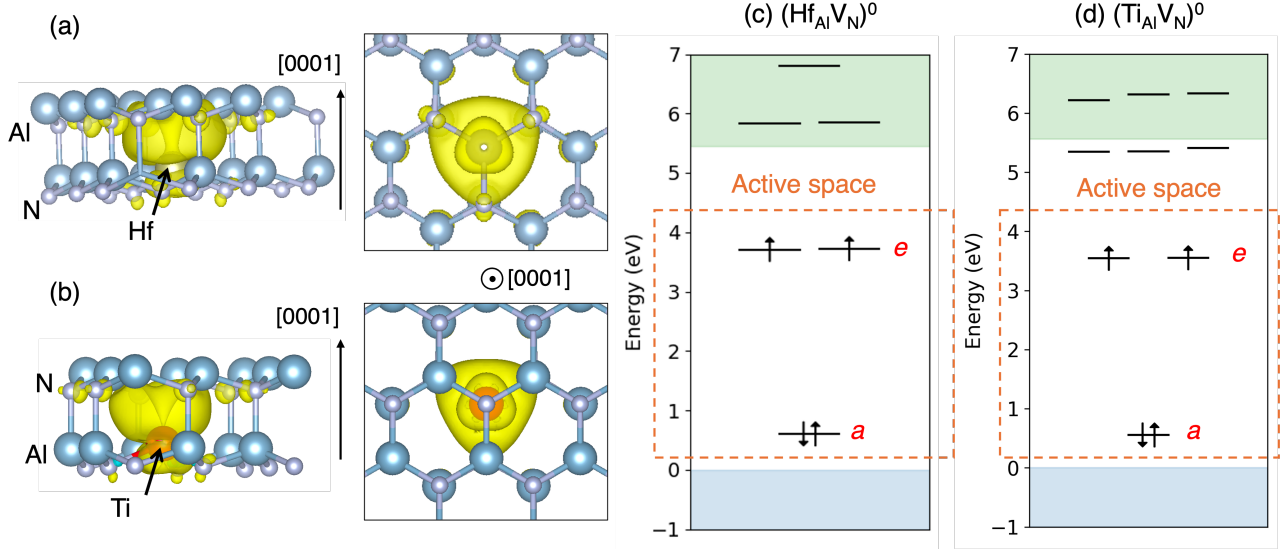


FIG. 11. Spin densities of (a) $(\text{Hf}_{\text{Al}}\text{V}_\text{N})^0$ and (b) $(\text{Ti}_{\text{Al}}\text{V}_\text{N})^0$ in w-AlN obtained by spin-unrestricted DFT calculations. Isosurfaces are displayed at 10% and 2.5% of the maximum values for $(\text{Hf}_{\text{Al}}\text{V}_\text{N})^0$ and (b) $(\text{Ti}_{\text{Al}}\text{V}_\text{N})^0$, respectively, in w-AlN. Kohn-Sham defect levels of (c) $(\text{Hf}_{\text{Al}}\text{V}_\text{N})^0$ and (d) $(\text{Ti}_{\text{Al}}\text{V}_\text{N})^0$ in w-AlN obtained by spin restricted DFT calculation. Orange dashed box denotes an energy region to take into account for constructing low-energy effective Hamiltonian.

The Pauli operators $\{P_\ell\}$ are the same, with only the coefficients $\{h_\ell\}$ differing depending on the system. The above generator is obtained by the function `Z2Symmetries` in `qiskit` v1.1.0 [111], which is applied to the low-energy effective Hamiltonian specified by the parameters in Table V after the Pauli transformation.

Appendix D: Numerical results of other vacancies

1. FCI calculations

We calculated other complex defects in *w*-AlN that are promising candidates for spin qubits. We selected the previously reported $(\text{Zr}_{\text{Al}}\text{V}_\text{N})^0$ [64, 65], $(\text{Ti}_{\text{Al}}\text{V}_\text{N})^0$ [64], and $(\text{Hf}_{\text{Al}}\text{V}_\text{N})^0$ [65] complexes in *w*-AlN. We used the same calculation settings for the DFT and RESPACK calculations, as in Sec. II A in main text.

The spin densities of $(\text{Hf}_{\text{Al}}\text{V}_\text{N})^0$ and $(\text{Ti}_{\text{Al}}\text{V}_\text{N})^0$ calculated from spin-polarized DFT calculations are presented in Fig. 11(a) and (b), respectively. The KS defect states obtained from spin-restricted DFT calculations are shown in Fig. 11(c) and (d), respectively. The results of the FCI calculations for the low-energy effective model constructed for the active space, framed by the orange dotted lines in Figures 11 (c) and (d), are summarized in Table VI.

TABLE VI. Energies (eV) calculated by FCI calculation for the complex defects in w-AlN. In cases where the FCI energy is slightly split, the energy of one of the two is given in brackets.

vacancy	functional	$^3A_2 \rightarrow ^3E$	$^3A_2 \rightarrow ^1A_1$	$^3A_2 \rightarrow ^1E$	$^1E \rightarrow ^1A_1$	$^1A_1 \rightarrow ^3E$
$(\text{Zr}_{\text{Al}}\text{V}_\text{N})^0$	PBE	2.39 (2.43)	0.86	0.43 (0.44)	0.43 (0.42)	1.54 (1.57)
	HSE	3.00 (3.04)	0.98	0.49 (0.5)	0.48 (0.49)	2.02 (2.06)
$(\text{Ti}_{\text{Al}}\text{V}_\text{N})^0$	PBE	2.53 (2.58)	0.87	0.43 (0.44)	0.43 (0.44)	1.66 (1.71)
	HSE	3.11 (3.12)	0.91	0.46 (0.47)	0.45 (0.45)	2.19 (2.21)
$(\text{Hf}_{\text{Al}}\text{V}_\text{N})^0$	PBE	2.42 (2.43)	0.85	0.44 (0.44)	0.41 (0.42)	1.57 (1.58)
	HSE	2.99 (3.00)	0.95	0.49 (0.49)	0.46 (0.47)	2.04 (2.04)

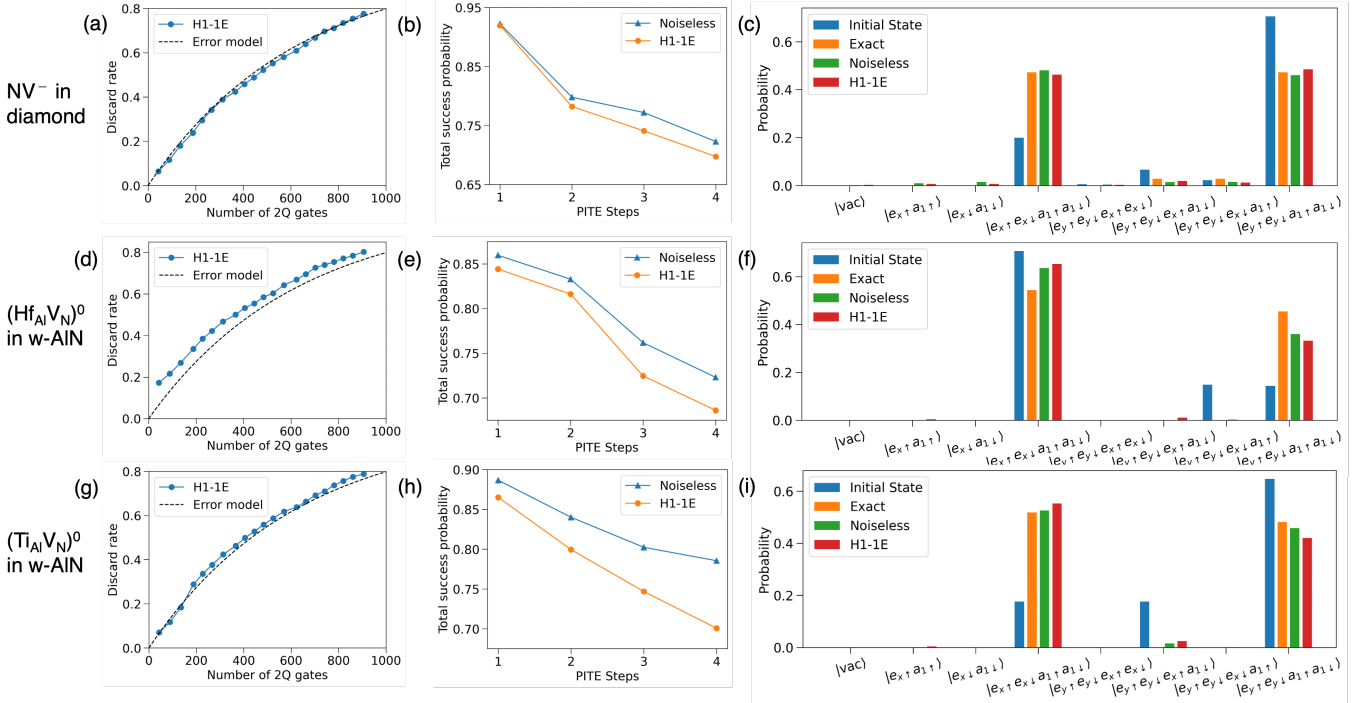


FIG. 12. Quantum computation of the ground state of the spin singlet state for (a-c) NV^- -center in diamond, (d-f) $(\text{Hf}_{\text{Al}}\text{V}_N)^0$ complex in w-AlN, and (g-i) $(\text{Ti}_{\text{Al}}\text{V}_N)^0$ complex in w-AlN. (a, d, g) Discard rates of the calculated results owing to errors detected by QED as a function of the number of two-qubit gates. The dashed line denotes noise model, as shown in Eq. (25) with $p_2 = 1.6 \times 10^{-3}$. (b, e, h) Total success probability of the PITE according to the PITE steps. (c, f, i) Histogram of measured computational basis. Noiseless denotes the noiseless simulation of PITE, and H1-1E denotes the emulator of H1-1 quantum computer. All calculations used $N_{\text{shot}} = 2000$.

2. Quantum computation of ground state of the singlet state

a. Trunction error on qubit reduction using \mathbb{Z}_2 symmetry

As in the case of the $(\text{Zr}_{\text{Al}}\text{V}_N)^0$ complex defects in w-AlN described in the main text, the truncation values of the Hamiltonians for $(\text{Hf}_{\text{Al}}\text{V}_N)^0$ and $(\text{Ti}_{\text{Al}}\text{V}_N)^0$ defects are small, at 0.01 eV and 0.005 eV, respectively. As a result, we did not observe any effect of truncation on the FCI energy at the second decimal point. On the other hand, the value of the truncation for NV centers in diamonds is somewhat large at 0.07 eV, and the FCI energy of the 1E state increases slightly from 0.64 eV to 0.7 eV. In this truncation, the many-body wave function of 1E state for NV-center diamond, presented in Table II in main text, is changed as

$$0.69(|e_{y\uparrow}e_{x\downarrow}a_{1\uparrow}a_{1\downarrow}\rangle - |e_{y\downarrow}e_{x\uparrow}a_{1\uparrow}a_{1\downarrow}\rangle) + 0.17(|e_{y\uparrow}e_{y\downarrow}e_{x\downarrow}a_{1\uparrow}\rangle - |e_{y\uparrow}e_{y\downarrow}e_{x\uparrow}a_{1\downarrow}\rangle) \quad (\text{D1})$$

and

$$0.69(|e_{x\uparrow}e_{x\downarrow}a_{1\uparrow}a_{1\downarrow}\rangle - |e_{y\uparrow}e_{y\downarrow}a_{1\uparrow}a_{1\downarrow}\rangle) + 0.17(|e_{y\downarrow}e_{x\uparrow}e_{x\downarrow}a_{1\uparrow}\rangle - |e_{y\uparrow}e_{x\uparrow}e_{x\downarrow}a_{1\downarrow}\rangle). \quad (\text{D2})$$

b. Ground-state calculation using emulator of H1-1

We present the computed results of the ground state of the singlet state on the emulator of H1-1 for the NV-center diamond in Fig. 12(a-c), HfV complex in w-AlN in Fig. 12(d-f), TiV complex in w-AlN in Fig. 12(g-i). The calculation conditions are the same as those described in Sec. III B of the main text, except that $N_{\text{shots}} = 2000$. The values of the calculation results in Figure 12 are summarized in Table VII.

TABLE VII. Computed results for the ground state of the spin singlet state for NV center in diamond, TiV in w-AlN, and HfV in w-AlN on the emulator of H1-1 (H1-1E).

System	Total success probability		Classical fidelity		Discard rate
	Noiseless	H1-1E	Noiselss	H1-1E	
NV^-	0.72	0.70	0.97	0.98	0.78
$(\text{Hf}_{\text{Al}}\text{V}_N)^0$	0.79	0.70	0.98	0.97	0.79
$(\text{Ti}_{\text{Al}}\text{V}_N)^0$	0.72	0.69	0.99	0.98	0.80